Kinematics and physical properties of the nearby galaxy NGC 4656 and its TDG candidate

N. Muñoz-Elgueta, S. Torres-Flores, P. Amram, J. A. Hernandez-Jimenez, F. Urrutia-Viscarra, C. Mendes de Oliveira, J. A. Gómez-López

Monthly Notices
of the
ROYAL ASTRONOMICAL SOCIETY

MNRAS **480,** 3257–3278 (2018)
Advance Access publication 2018 July 20

doi:10.1093/mnras/sty1934

Kinematics and physical properties of the nearby galaxy NGC 4656 and its TDG candidate

N. Muñoz-Elgueta,[1★] S. Torres-Flores,[1] P. Amram,[2] J. A. Hernandez-Jimenez,[3] F. Urrutia-Viscarra,[4] C. Mendes de Oliveira[3] and J. A. Gómez-López[2]

[1]*Departamento de Física y Astronomía, Universidad de La Serena, Av. Cisternas 1200, La Serena, Chile*
[2]*Aix Marseille Univ., CNRS, CNES, LAM (Laboratoire d'Astrophysique de Marseille), F-13388, Marseille, France*
[3]*Instituto de Astronomia, Geofísica e Ciências Atmosféricas, Universidade de São Paulo, 05508-900 São Paulo, Brazil*
[4]*Gemini Observatory/AURA, Southern Operations Center, Casilla 603 La Serena, Chile*

Accepted 2018 July 18. Received 2018 July 17; in original form 2018 June 14

ABSTRACT

Interacting galaxies provide us with an excellent laboratory for studying a number of physical phenomena associated with these processes. In this paper, we present a spectroscopic and kinematic analysis of the interacting galaxy NGC 4656 and its companion tidal dwarf galaxy (TDG) candidate, NGC 4656UV. Using Fabry–Perot and GMOS multislit data, we investigated the possible origin of NGC 4656UV. We found that NGC 4656UV has a low metallicity ($12+\log(\mathrm{O/H})\sim8.2$) and it follows the mass–metallicity relation for normal dwarf galaxies. For NGC 4656, we estimated a flat oxygen abundance gradient of $\beta = -0.027 \pm 0.029$ dex kpc^{-1}, which suggests the presence of gas flows induced by gravitational interactions. By analysing radial velocity profiles and by fitting a kinematic model of the observed velocity field, we confirm the literature result that NGC 4656 consists of one single body instead of two objects. We estimated a dynamical mass of $6.8^{1.8}_{-0.6} \times 10^9$ M$_\odot$ and R of 12.1 kpc from the kinematic model of NGC 4656. Although the observed velocity field is dominated by rotation at large scales ($V_{\mathrm{max}}/\sigma \gtrsim 2.8$), important non-rotational motions are present at small scales. Based on these new results, and on previously published information, we propose that NGC 4656 and 4656UV are a pair of interacting galaxies. NGC 4656UV is a companion of NGC 4656 and it does not have a tidal origin. The interaction between the two could have triggered the star formation in NGC 4656UV and increased the star formation in the north-east side of NGC 4656.

Key words: galaxies: dwarf – galaxies: individual (NGC 4656) – galaxies: interactions – galaxies: kinematics and dynamics.

1 INTRODUCTION

The hierarchical scenario of galaxy formation argues that the interactions and mergers play a fundamental role, and they are the key to the growth of the structures observed today (e.g. Toomre & Toomre 1972; Kauffmann & White 1993). Morphology, kinematic, metallicity, and other physical properties are affected by interactions during galaxy evolution. For example, in the case of galaxy pairs, since Toomre & Toomre 1972 we know that due to the intense tidal forces, interacting galaxies often show elongated and extended tidal tails, which are composed by stars and interstellar gas. On the other hand, several authors have studied the oxygen abundances in the discs of galaxies with star formation and in tidal tails of interacting systems (e.g. Rich et al. 2012; Torres-Flores et al. 2014), finding metallicity gradients flatter than in isolated systems (e.g. Zaritsky, Kennicutt & Huchra 1994). This is consistent with results obtained in numerical simulations, which show that gas flows induced by interactions redistribute the gas in such a way that the original abundance gradients present in the galactic discs progressively flatten as the interaction/merger stage progresses (Rupke, Kewley & Barnes 2010a; Torrey et al. 2012). Other most common indicators of ongoing interactions, from the galaxies kinematics, are highly disturbed velocity fields, presence of non-circular motions, double nuclei, double components in the emission profiles that trace the gas, the presence of an anomalous kinematic structures, misalignment of the position angles of the stellar and gaseous major axes, and a discordance between approaching and receding sides of the rotation curve (Amram et al. 2003).

★ E-mail: nahir@dfuls.cl

An important and (by now) well-known end-result of tidal interactions is the possible formation of new stellar systems. For example, if the expelled material from interacting galaxies is gravitationally bound, the formation of a tidal dwarf galaxy (TDG) is possible. First suggestions that new objects may be produced when galaxies collide remote from 1956, with Zwicky and more recently by Hibbard & van Gorkom (1996). Duc & Mirabel (1998) showed that newly formed objects in interacting/merging galaxies have high metallicities because they formed from material already enriched by previous generations of stars in the disc of the galaxy. TDGs are born in gaseous clouds/tails produced by interaction events; they are embedded in reservoirs of enriched cold gas and are expected to be active by forming stars. To be defined as TDGs, these newly formed objects must be self-gravitating (Duc & Mirabel 1999; Duc et al. 2011; Duc 2012). Since TDGs are formed by gas ejected from the disc of gas-rich galaxies, this new class of objects may not contain a halo of dark matter, fact that fundamentally differentiates them from primordial dwarf galaxies, which have high M/L (Bournaud 2010). The fate of TDGs in the context of galaxy evolution is not yet well understood. With time, TDGs could be converted into satellite galaxies (Hunsberger, Charlton & Zaritsky 1996), but it is not yet clear if the TDGs can survive the intense tidal field and the energetic feedback produced by the formation and stellar evolution within them (Ploeckinger et al. 2015). The existence of evolved TDGs has been suggested by Duc et al. (2014). If these objects survive, they could be part of the population of dwarf galaxies. In order to understand TDGs formation and physical properties of progenitor galaxies, detailed studies of interacting systems exhibiting TDG candidates are requested, motivating the current study.

The system that is the subject of the present study consists of a galaxy, NGC 4656 and a TDG candidate called NGC 4656UV, which are part of a larger group where NGC 4631 and NGC 4656 are the main galaxies. NGC 4656 is classified as a SB(s)m pec galaxy located at a distance of 5.1 Mpc (Sorce et al. 2014, redshift-independent distance measured with Tully–Fisher) and shows a disturbed morphology that displays obvious signs of gravitational interaction. In literature, several authors have studied this system, however, the nature of NGC 4656 and the origin of NGC 4656UV are still unclear. In order to continue the investigation on the most probable scenario for the formation and evolution of these objects, in this paper we have obtained Gemini GMOS spectroscopic data and Fabry–Perot (FP) data suitable for a thorough kinematic study of the system. In Section 2, we present the system to study, the data description, and reduction. The data analysis are presented in the Sections 3 and 4. In Section 5, we present our results, continuing with discussion and conclusions that are presented in Sections 6 and 7, respectively.

2 THE SYSTEM AND OBSERVATIONAL DATA

2.1 NGC 4656 and its TDG candidate, NGC 4656UV

The galaxy pair NGC 4656/NGC 4631 has been studied by several authors, and different scenarios have been proposed about its nature. The bright north-east end of NGC 4656 has also been cataloged as NGC 4657; hence, some authors refer to this system as NGC 4656/4657. A few authors (de Vaucouleurs & de Vaucouleurs 1964; Nilson 1973) consider that NGC 4657 is a separate entity from NGC 4656. de Vaucouleurs & de Vaucouleurs (1964) proposed that the system could consist of two irregular magellanic interacting galaxies, possibly similar to the antennae glaxies. On the other hand, Burbidge, Burbidge & Shelton (1967) found that NGC 4656 resembles structurally to MCG 12-7-28, concluding that it may be a barred spiral with a weak arm. Subsequently, Roberts (1968) shows the distribution and content of neutral hydrogen for the NGC 4656/4631 pair, finding a neutral atomic hydrogen bridge connecting NGC 4656 and NGC 4631, suggesting that the gas has been expelled by NGC 4631 because of its gravitational interaction with NGC 4656. One decade later this bridge was resolved by Weliachew, Sancisi & Guelin (1978) who, using 21 cm hydrogen line observations, found that the bridge is composed mainly by two filamentary structures. A different scenario was proposed by Nilson (1973), who considered that NGC 4657 could be a separate object superimposed onto NGC 4656. However, by analysing surface brightness profiles, Stayton, Angione & Talbert (1983) concluded that NGC 4656 and NGC 4657 were part of the same galaxy, and found no conclusive optical indicators indicating an interaction with their neighbor NGC 4631. By studying the HI gas, Rand (1994) note that NGC 4656 presents a structure that is disturbed and they concluded it is due to interaction effects. They suggested that NGC 4656 could be a system with two loosely wrapped tidal arms, or a ring galaxy almost edge-on.

It is only in the work of Schechtman-Rook & Hess (2012) where it was announced the discovery of a TDG candidate in the NGC 4656 system, which was denominated NGC 4656UV. Through evolutionary synthesis models, they found that NGC 4656UV presents a low metallicity (∼10 times smaller than NGC 4656), and associated the origin of this TDG candidate to an encounter between NGC 4656 and NGC 4631 about 260–290 Myr ago. de Mello et al. (2012) confirmed that this object could be a TDG candidate in finding 8 UV sources with ages less than 100 Myr. On the other hand, a giant stellar tidal stream was discovered in the halo of NGC 4631, a part of which extends between NGC 4631 and NGC 4656 (Martínez-Delgado et al. 2015). However, these authors discarded that the origin of this stream is due to some previous interaction between these two galaxies, mainly because the inclination of NGC 4631 and NGC 4656 with respect to the orbital plane makes tidal formation inefficient. They suggested that the streams around NGC 4631 are results of interactions between this galaxy and its dwarf satellites.

The main properties of NGC 4656 and NGC 4656UV are summarized in Table 1.

2.2 GMOS Data

Spectroscopic observations were collected with the Gemini Multi-Object Spectrograph (GMOS; Hook et al. 2004) mounted on the Gemini North telescope in multislit mode, during the nights of 2013 May 11 and June 1 under the science programme GN-2013A-Q-87 (PI: F. Urrutia-Viscarra). Since one of our goals is to study the physical properties of the system based on strong-line methods, we used *GALEX* images for the whole system to select the bluest star-forming regions in NGC 4656 and its TDG candidate. After selecting the regions, we proceeded to build the multislit masks. For this purpose, four images of 300 s each were obtained in the g'-band filter for three different fields: one of them includes the whole TDG candidate and other two cover the north-east and the south-west regions of NGC 4656.

These images were processed with the Gemini IRAF package (version 1.8), and the final combined images were used to build the multislit masks. Considering that our sources are mostly point like, we adopted slit widths of 1 arcsec to maximize the incoming light and to match the seeing. In order to improve the number of observed star-forming regions and the local sky sampling, the lengths of the

Table 1. Main properties of the sample.

ID	α(2000) (h:m:s)	δ(2000) (d:m:s)	V_{syst} (km s^{-1})	Distance (Mpc)	Size (arcmin)	M ($M_\odot$)	$M_{H\,I}$ ($M_\odot$)	M_{dyn} ($M_\odot$)	SFR ($M_\odot$ yr^{-1})
NGC 4656	12:43:57.73[a]	+23:10:05.30[a]	646[a]	8.21[a]	12.88[a]	–	1.7×10^{9}[b]	1.9×10^{10}[c]	0.666[c]
TDG candidate	12:44:14.79[c]	+32:16:48.26[c]	570[c]	8.21[a]	4.93[c]	9×10^{7}[c]	3.8×10^{8}[c]	1.6×10^{9}[c]	0.027[c]

[a]Values were taken from NED.
[b]Values were taken from Weliachew et al. (1978).
[c]Values were taken from Schechtman-Rook & Hess (2012).

slits were set for each object individually. The orientations of all slits are according to the instrumental position angle of 0° for TDG candidate, 43° for the field over NGC 4656 north-east (hereafter Target 1) and 258° for the field over NGC 4656 south-west (hereafter Target 2). In total, 52 regions with FUV emission were observed in Target 1, 48 in Target 2, and 30 in NGC 4656UV. Fig. 1 shows a false colour image of NGC 4656 and NGC 4656UV combined using the FUV, FUV+NUV and NUV filters from GALEX. Over this image red crosses have been superimposed representing the observed regions which do not present Hα emission. The orange boxes correspond to zooms of the GMOS images observed in the g'-band. The red rectangles with numbers represent the slits used, which contain only regions that have at least the Hα emission line in their spectra, and that are at the redshift of the system ($z \sim 0.002$). From here on, we will refer only to the spectra of these regions, since these were used to measure physical properties. The positions of these regions are presented in Table 3.

The observations were taken by using the grating R400_G5305 and were performed taking exposures of 1570, 1300, and 1345 s for the TDG candidate, Target 1 and Target 2 respectively in three different central wavelengths: 6450, 6500, and 6550 Å for each target. The spectral coverage ranged typically from 4700 to 7700 Å, which allowed us to measuring the emission lines necessary to estimate the physical properties of the system (Hβ, [O III] $\lambda\lambda$ 4959, 5007, Hα, [N II] $\lambda\lambda$ 6548, 6584, [S II] $\lambda\lambda$6716, 6731). The spectral resolution at Hα was $R \sim 875$ ($\Delta\lambda \sim 7.5$). Flat-field frames were taken after each science observation in order to avoid any effect caused by the instrumental flexure, and CuAr arc lamps spectra were observed at the end of each night.

2.2.1 *Data reduction and flux calibration*

The GMOS data were reduced using the GEMINI package version 1.13.1 in IRAF. All frames were bias subtracted, trimmed, and flat-fielded using GBIAS, GSFLAT and GSREDUCE. Cosmic rays were removed using LACOS_SPEC (van Dokkum 2001). Each individual 2D spectrum, corresponding to one slit for each central wavelength observed, was cut from the MOS field using the task GSCUT. All spectra were wavelength calibrated using the tasks GSWAVELENGTH and GSTRANSFORM. The rms value of the wavelength calibration was ~0.3 Å for each target. The combination of the three spectra taken at slightly different central wavelengths was done in order to remove the detector gaps and the cosmic rays that were still present, using the task GCOMBINE. The sky lines were removed with the task GSSKYSUB. Then, with the purpose to flux calibrate all spectra, similar procedures were applied to the spectrum of the standard star Wolf 1346. The sensitivity function was obtained with the task SENSFUNC. The standard star Wolf 1346 was observed on a different night from that of the main fields on 2013 June 2. Finally, we obtained calibrated unidimensional spectrum for each region observed in NGC 4656 and NGC 4656UV.

2.3 FP data

The two-dimensional kinematic observations of NGC 4656 and the TDG candidate were carried out 2016 March 2–6, using the GHASP instrument that consists of a focal reducer containing a FP interferometer, interference filters, and an imaging photon counting system (IPCS). GHASP is mounted on the Cassegrain focus of the 1.93 m telescope at the Observatoire de Haute Provence (OHP). The field of view (FoV) of the instrument is ~5.8 × 5.8 arcmin^2 and the IPCS detector (Gach et al. 2002) provides a pixel size of 0.68 arcsec pix^{-1}. The interference order of the FP used was $p = 798$ at Hα, where the free spectral range (FSR) was 376 km s^{-1}. The Finesse of the interferometer is $F = 12$, and in order to sample correctly the line, we scanned the FSR through 32 channels, hence the sampling step is about 12 km s^{-1}. A total exposure time of 10.4 h was distributed over 11 overlapping FoVs mapping the whole system, two of them corresponding to the TDG candidate and nine to NGC 4656. In order to minimize sky variation during the scanning process, thanks to the IPCS that is read-out noise free, each individual channel was observed with an exposure time of 10 s. The total observing time per field range between 1920 and 8940 s (see Table 2).

2.3.1 *Data reduction*

The FP data were reduced by using the package developed by Daigle et al. (2006). This reduction package provides spatial adaptive binning, based on the 2D Voronoi tessellation method, applied to the 3D data cubes. The spatial adaptive binning allows to keep the highest spatial resolution in bright H II regions, meanwhile it increases the signal-to-noise ratio (SNR) in low-flux areas in decreasing the spatial resolution. Using this technique, bins are formed by adding new pixels until the region reaches a given level that is set a prior; this level is known as the signal-to-noise target (SNRt). For NGC 4656, we set SNRt = 5 per bin. Nevertheless, the TDG candidate displays such a low Hα emission over all its extension that the adaptative binning used for NGC 4656 is not suitable for the TDG candidate; thus, we applied a Gaussian smoothing with a full width at half-maximum of 3 pixels. Astrometry was provided by using the KOORDS routine of the KARMA package (Gooch 1996).

Sky emission was removed through the subtraction of a sky cube, built from regions with no emission from the associated galaxies. Once the reduction process is finished, we obtain the Hα monochromatic map, the velocity field, and the velocity dispersion map for each field observed. These maps were finally cleaned through the routine CLEAN_MAPS, where the low-intensity emission associated with instrumental noise was subtracted.

For each field, velocity dispersion maps obtained have been corrected from instrumental broadening. In this way, the real velocity dispersions σ can be estimated through $\sigma = \sigma^2_{observed} - \sigma^2_{inst}$, assuming that the observed and instrumental profiles can be fitted by Gaussian functions. The instrumental broadening was estimated from the

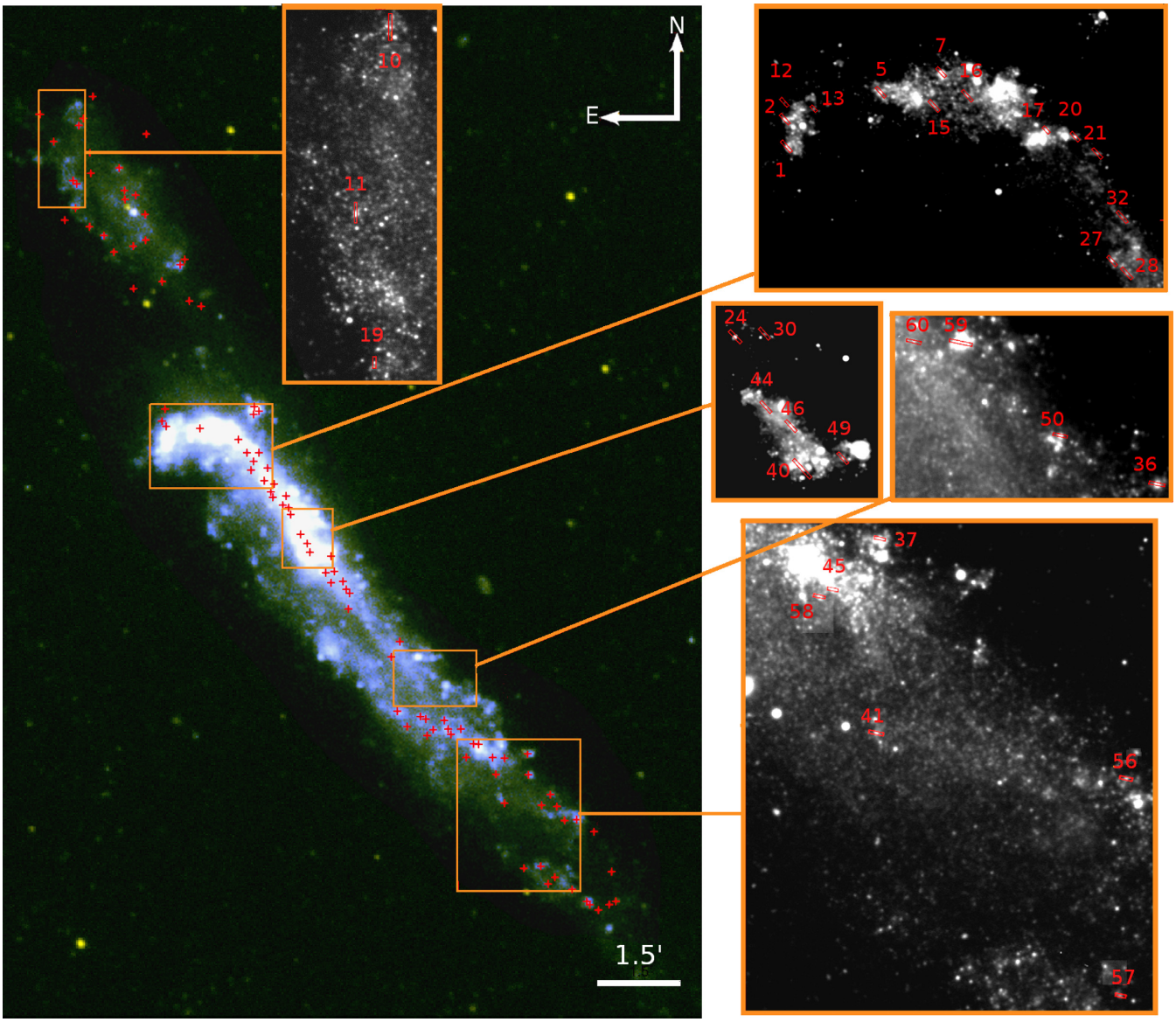

Figure 1. False colour image of NGC 4656 in the FUV and NUV bands (observed with *GALEX*), where FUV represents the blue, the sum of FUV + NUV the green, and NUV the red. The red rectangles represent the slits used in GMOS observations, whose regions present spectra with emission lines. Each one is positioned with its respective orientation angle. The numbers on the slits indicate the identification of each region. The red crosses represent the GMOS regions that do not present H α emission.

average of dispersion maps derived from the lines of the neon calibration lamp, whose resulting value was $\sigma_{\rm inst} = 11.5 \pm 5.0\,{\rm km\,s^{-1}}$, where the uncertainty is represented by the standard deviation.

2.3.2 *Flux calibration*

H α monochromatic maps were flux calibrated by using the Gemini GMOS spectra. With this purpose, we have used the H α flux of a total of 34 sources (where 3 sources are located in the TDG candidate, and 31 in NGC 4656). On the other hand, we have used the monochromatic FP maps to estimate the H α emission (in counts s^{-1}) in the same extraction windows used for the Gemini data. Then, we compared the H α fluxes (in erg $s^{-1}cm^{-2}$) with the H α emission measured for the FP data by fitting a linear fit on the data and fixing the zero-point equal to zero. The final fit provided us a coefficient of 2.19×10^{-17} erg count^{-1} cm^{-2}that was used to calibrate the H α monochromatic maps for NGC 4656 and the TDG candidate. The root mean square error (RMSE) of the linear relation is 1.32×10^{-15}erg $s^{-1}cm^{-2}$.

3 SPECTROSCOPY: PHYSICAL PARAMETERS

3.1 Extinction

The spectra of the regions observed with GMOS show negligible stellar continuum compared with the strong emission from the nebular lines. Since the observed emission is affected by Galactic and internal extinction, it is necessary to make corrections. The observed fluxes were corrected for Galactic extinction through the IDL code FM_UNRED (Fitzpatrick 1999), using a colour excess of $E(B - V) = 0.011$ (NASA/IPAC Extragalactic Database). There is a different internal extinction for each region, since it depends on

Table 2. Central coordinates and exposure times of the observed FP fields.

ID[a]	RA[b] (J2000)	Dec.[b] (J2000)	t^{c}_{exp} (s)
1	12:44:18	+32:16:50	8965
2	12:44:14	+32:14:40	3780
3	12:44:14	+32:13:20	1920
4	12:44:10	+32:11:50	1980
5	12:44:06	+32:10:40	1980
6	12:44:03	+32:09:50	1980
7	12:43:59	+32:08:40	1980
8	12:43:55	+32:07:30	1980
9	12:43:50	+32:06:30	1980
10	12:43:43	+32:04:30	3480
11	12:43:34	+32:03:10	7380

[a]Identification number for each observed field (north-south direction).
[b]Central coordinates of the field, in J2000 epoch.
[c]Total exposure time for each field, in seconds.

the internal properties of each source. The spectral coverage of our observations allows us to derive the H α/H β ratio to determine the internal extinction through the Balmer decrement. We have computed intrinsic H α/H β ratio in referring to Osterbrock & Ferland (2006), considering a typical electronic temperature and density for H II regions of $T_e = 10\,000$ K and $N_e = 100$ cm^{-3}. We consider hereafter this value as a lower threshold. Then, the observed fluxes for all spectra were corrected for internal reddening using the IDL code CALZ_UNRED (Calzetti et al. 2000), which assumes a starburst extinction law. We have first estimated the nebular colour excess following the recipes given in Domínguez et al. (2013), and then we obtained the stellar colour excess that in this case is expressed by $E(B-V)_{star} = 0.44 \times E(B-V)_{gas}$. The sources for which H β emission was not detected (regions #10, 11, 12, 44, 45, 50, 56, 57, 58, and 60) and those for which H α/H β ratio was lower than the intrinsic value defined above (regions #1, 40, 13, and 37, with emission lines contaminated by noise) were not corrected by internal extinction because it was not possible to estimate $E(B-V)_{star}$. The values of the colour excesses, for the regions in which this measurement was possible, are listed in the third column of Table 3.

3.2 Emission-line measurements

Once the spectra were corrected by extinction, we measured the nebular emission-line fluxes corresponding to H β, [O III] $\lambda\lambda$4959, 5007, H α, [N II] $\lambda\lambda$6548, 6584, and [S II] $\lambda\lambda$6716, 6731. We have used the SPLOT task in the NOAO package from IRAF, fitting Gaussian models to the emission lines. The SPLOT task provides uncertainties for the fluxes measurements, which are computed by Monte Carlo simulation. In Table 3, we tabulate the fluxes and their uncertainties for each region observed with GMOS.

3.3 Oxygen abundances and radial distances

In order to determine the behaviour of the metallicity in the system NGC 4656, from GMOS fluxes we have estimated the oxygen abundances using semi-empirical methods through the N2 and O3N2 calibrators, given that our data does not cover the spectral region of temperature sensitive [O III] λ4363 emission line. We used the calibrations proposed by Marino et al. (2013), who provided linear relations to obtain oxygen abundances through the N2 and O3N2 calibrator, with an accuracy of 0.16 and 0.18 dex, respectively. Uncertainties in the oxygen abundances have been calculated by propagating the flux uncertainties and adding in quadrature the 0.16/0.18 dex value associated with the scatter in the calibration. The results are shown in detail for each region in Table 4.

The projected galactocentric distances to each star-forming region in NGC 4656 were estimated following the method of Scarano et al. (2008). Given the high inclination of this system ($i = 82°$; Stayton et al. 1983), distances were not corrected by inclination. In the case of the position angle, we used a value of PA = 40° (taken from Schechtman-Rook & Hess 2012), which corresponds to the position angle of the major axis seen on Fig. 1.

Although a normalization of the galactocentric distance (e.g. to the optical radius R_{25}) is useful to compare the metal distributions between different galaxies, we adopt an absolute radial scale (dex kpc^{-1}) for NGC 4656 since this object presents a very disturbed morphology with tidal characteristics, for which the chosen scale has a greater physical significance in this particular case. The results for the projected distances and their respective uncertainties calculated from the uncertainty in the scale of the distance to the source ($\sim 0.024 \pm 0.005$ kpc arcsec^{-1}) are listed in the second column of Table 4.

3.4 Electron densities

The electron densities were calculated from the observed [S II] $\lambda\lambda$6716, 6731 ratio (hereafter RS2) using the task TEMDEN, in the STSDAS NEBULAR package from IRAF. All the tasks in this package implement the five-level atomic model FIVEL, developed by De Robertis, Dufour & Hunt (1987). Since we are not able to estimate the electron temperature because of the spectral coverage, we assumed an electronic temperature of $T_e = 10\,000$ K, which is expected for star-forming regions (Osterbrock & Ferland 2006). The values of the electron densities and their respective uncertainties (given by the standard deviation) are presented in the last column of Table 4.

3.5 Star formation rates

There are different star formation rate (SFR) indicators, one of them is the H α nebular emission that emerges from the recombination of gas that has been ionized by the population of most massive stars (O and B stars). This indicator traces star formation over the few last million years. From our flux calibrated FP data, the SFRs for NGC 4656 and its TDG candidate have been estimated through their H α luminosity, using the expression given in Kennicutt (1998), where

$$\mathrm{SFR}_{\mathrm{H}\alpha} = 7.94 \times 10^{-42} \times L(\mathrm{H}\alpha), \quad (1)$$

assuming a continuous star formation process. It is important to note that this SFR can be underestimated due to the fact that H α is affected by extinction. In our case, H α maps have not been corrected by extinction which is variable along the extension of the systems. The uncertainties in the luminosities have been estimated propagating the errors of the fluxes, and considering an uncertainty in the distance to NGC 4656 of 1.1 Mpc (Sorce et al. 2014). For the SFRs, the uncertainties were derived propagating the errors for luminosities. These results are presented in Tables 5 and 6.

4 KINEMATICS

4.1 Rotation curves

The rotation curves (RCs) through the classical method for different regions of NGC 4656 were computed with the software ADHOCw,

Table 3. Positions, fluxes and colour excesses for star-forming regions in NGC 4656 and NGC 4656UV.

ID	RA (J2000)	Dec (J2000)	$E(B-V)^a_{\rm est}$	H β	[O III]λ4959	[O III]λ5007 ($\times 10^{-15}$erg)	H α (cm^{-2}s^{-1})	[N II]λ6548	[N II]λ6584	[S II]λ6716	[S II]λ6731
1	12:44:11.513	+32:12:14.37	–	0.059 ± 0.004	0.040 ± 0.004	0.076 ± 0.006	0.141 ± 0.004	0.004 ± 0.006	0.007 ± 0.006	0.012 ± 0.005	0.008 ± 0.007
2	12:44:11.564	+32:12:23.65	0.073	1.900 ± 0.028	1.890 ± 0.028	5.630 ± 0.032	6.330 ± 0.029	0.066 ± 0.052	0.224 ± 0.036	0.265 ± 0.033	0.192 ± 0.035
5	12:44:09.003	+32:12:32.76	0.050	1.600 ± 0.029	1.660 ± 0.028	4.890 ± 0.025	4.940 ± 0.024	0.038 ± 0.050	0.131 ± 0.034	0.321 ± 0.027	0.244 ± 0.033
7	12:44:07.389	+32:12:39.39	0.134	1.380 ± 0.008	1.980 ± 0.008	5.800 ± 0.008	4.690 ± 0.008	0.066 ± 0.010	0.134 ± 0.009	0.223 ± 0.009	0.158 ± 0.010
10	12:44:19.416	+32:18:44.89	–	–	–	–	0.043 ± 0.004	–	–	–	–
11	12:44:20.343	+32:17:41.99	–	–	–	–	0.207 ± 0.009	–	–	0.012 ± 0.013	0.008 ± 0.020
12	12:44:11.568	+32:12:29.31	–	–	–	–	0.090 ± 0.007	–	–	0.014 ± 0.011	–
13	12:44:10.788	+32:12:27.18	–	0.167 ± 0.015	–	–	0.329 ± 0.006	–	–	–	–
15	12:44:07.575	+32:12:28.16	0.034	0.216 ± 0.018	0.246 ± 0.019	0.482 ± 0.016	0.598 ± 0.016	0.015 ± 0.035	0.029 ± 0.021	0.047 ± 0.019	0.036 ± 0.019
16	12:44:06.692	+32:12:31.58	0.007	0.590 ± 0.021	0.319 ± 0.019	1.030 ± 0.020	1.720 ± 0.019	0.021 ± 0.024	0.063 ± 0.021	0.117 ± 0.022	0.084 ± 0.021
17	12:44:04.581	+32:12:20.01	0.052	0.678 ± 0.027	1.020 ± 0.025	2.920 ± 0.026	2.090 ± 0.027	0.041 ± 0.140	0.035 ± 0.030	0.085 ± 0.030	0.053 ± 0.028
19	12:44:19.845	+32:16:51.42	0.119	0.257 ± 0.018	0.289 ± 0.015	0.826 ± 0.015	0.917 ± 0.016	–	–	0.036 ± 0.019	0.028 ± 0.021
20	12:44:03.812	+32:12:17.74	0.178	0.724 ± 0.044	0.947 ± 0.044	2.950 ± 0.042	2.880 ± 0.038	–	0.115 ± 0.063	0.165 ± 0.063	0.140 ± 0.062
21	12:44:03.225	+32:12:12.10	0.064	1.520 ± 0.026	1.590 ± 0.031	4.750 ± 0.029	4.780 ± 0.028	0.037 ± 0.040	0.161 ± 0.030	0.245 ± 0.029	0.175 ± 0.031
24	12:43:59.918	+32:10:51.67	0.031	4.880 ± 0.031	6.330 ± 0.030	19.100 ± 0.030	14.200 ± 0.029	0.154 ± 0.036	0.523 ± 0.033	0.580 ± 0.032	0.455 ± 0.033
27	12:44:02.830	+32:11:35.80	0.149	1.230 ± 0.033	2.020 ± 0.033	5.850 ± 0.031	4.480 ± 0.030	0.043 ± 0.040	0.136 ± 0.038	0.165 ± 0.028	0.143 ± 0.032
28	12:44:02.435	+32:11:31.49	0.098	0.493 ± 0.023	0.793 ± 0.024	2.340 ± 0.025	1.810 ± 0.024	0.022 ± 0.049	0.075 ± 0.025	0.210 ± 0.025	0.147 ± 0.023
30	12:43:59.136	+32:10:52.71	0.052	1.210 ± 0.027	0.906 ± 0.027	2.620 ± 0.028	3.830 ± 0.026	0.090 ± 0.026	0.244 ± 0.026	0.341 ± 0.028	0.235 ± 0.024
32	12:44:02.555	+32:11:50.53	0.056	0.684 ± 0.019	0.754 ± 0.021	2.110 ± 0.021	2.230 ± 0.022	0.039 ± 0.031	0.083 ± 0.026	0.119 ± 0.021	0.090 ± 0.021
36	12:43:43.583	+32:07:24.89	0.062	0.135 ± 0.036	0.221 ± 0.036	0.585 ± 0.037	0.463 ± 0.027	–	–	0.027 ± 0.110	0.017 ± 1.300
37	12:43:41.297	+32:06:36.43	–	0.161 ± 0.009	0.052 ± 0.006	0.171 ± 0.007	0.406 ± 0.007	0.006 ± 0.027	0.005 ± 0.007	0.023 ± 0.008	0.012 ± 0.008
40	12:43:58.130	+32:10:07.00	–	0.295 ± 0.019	0.343 ± 0.018	1.230 ± 0.017	0.795 ± 0.020	–	0.047 ± 0.021	0.076 ± 0.023	0.054 ± 0.024
41	12:43:41.396	+32:05:30.73	0.049	0.239 ± 0.011	0.179 ± 0.011	0.440 ± 0.011	0.744 ± 0.011	–	0.014 ± 0.020	0.023 ± 0.012	0.018 ± 0.015
44	12:43:59.098	+32:10:27.88	–	–	–	0.044 ± 0.006	0.073 ± 0.004	–	0.010 ± 0.008	0.016 ± 0.0056	0.014 ± 0.009
45	12:43:42.553	+32:06:19.29	–	–	–	–	0.049 ± 0.004	–	–	–	–
46	12:43:58.432	+32:10:21.47	0.059	2.070 ± 0.025	4.160 ± 0.028	12.700 ± 0.025	6.360 ± 0.024	0.044 ± 0.058	0.085 ± 0.029	0.190 ± 0.028	0.148 ± 0.031
49	12:43:57.048	+32:10:10.56	0.138	1.810 ± 0.047	3.010 ± 0.043	8.870 ± 0.047	6.180 ± 0.042	0.068 ± 0.042	0.130 ± 0.055	0.234 ± 0.051	0.153 ± 0.040
50	12:43:46.162	+32:07:41.30	–		–	–	0.043 ± 0.008	–	–	–	–
56	12:43:34.739	+32:05:15.36	–	–	–	–	0.145 ± 0.007	–	–	–	–
57	12:43:34.897	+32:04:01.92	–	–	–	–	0.020 ± 0.008	–	–	–	–
58	12:43:42.910	+32:06:16.89	–	–	–	–	0.079 ± 0.010	–	–	–	–
59	12:43:48.812	+32:08:12.76	0.041	7.480 ± 0.050	15.700 ± 0.045	49.100 ± 0.048	21.800 ± 0.048	0.082 ± 0.076	0.255 ± 0.052	0.593 ± 0.053	0.410 ± 0.051
60	12:43:50.069	+32:08:13.23	–	–	–	–	0.087 ± 0.011	–	–	–	–

[a]Internal stellar colour excess for each source, estimated according to Calzetti et al. (2000).

Table 4. Distances, oxygen abundances, and electron densities for H II located in NGC 4656.

ID	Distance[a] (kpc)	N2	O3N2	12 + log(O/H)[b]	12 + log(O/H)[c]	RS2[d]	N_e (cm^{-3})
1	5.22 ± 1.15	-1.27 ± 0.33	1.39 ± 0.34	8.15 ± 0.23	8.24 ± 0.20	1.33	94
2	5.36 ± 1.18	-1.45 ± 0.07	1.92 ± 0.07	8.07 ± 0.17	–	1.37	54
5	4.93 ± 1.09	-1.58 ± 0.11	2.06 ± 0.11	8.01 ± 0.18	–	1.31	110
7	4.73 ± 1.04	-1.54 ± 0.03	2.17 ± 0.03	8.03 ± 0.17	–	1.41	16
15	4.55 ± 1.01	-1.32 ± 0.32	1.66 ± 0.32	8.13 ± 0.22	8.18 ± 0.19	1.33	90
16	4.45 ± 0.98	-1.44 ± 0.14	1.67 ± 0.15	8.08 ± 0.18	8.17 ± 0.18	1.38	40
17	3.85 ± 0.85	-1.77 ± 0.37	2.40 ± 0.37	–	–	1.59	<10
20	3.68 ± 0.81	-1.39 ± 0.24	2.01 ± 0.24	8.09 ± 0.20	–	1.17	275
21	3.47 ± 0.77	-1.47 ± 0.08	1.97 ± 0.08	8.06 ± 0.17	–	1.41	19
24	1.30 ± 0.29	-1.43 ± 0.03	2.03 ± 0.03	8.08 ± 0.17	–	1.26	160
27	2.67 ± 0.59	-1.52 ± 0.12	2.19 ± 0.12	8.04 ± 0.18	–	1.15	304
28	2.52 ± 0.56	-1.38 ± 0.14	2.06 ± 0.15	8.10 ± 0.18	–	1.43	<10
30	1.21 ± 0.27	-1.19 ± 0.05	1.53 ± 0.05	8.19 ± 0.17	8.21 ± 0.18	1.45	<10
32	2.92 ± 0.65	-1.43 ± 0.14	1.92 ± 0.14	8.08 ± 0.18	–	1.32	98
40	0.13 ± 0.03	-1.23 ± 0.19	1.85 ± 0.20	8.17 ± 0.19	–	1.39	37
44	0.68 ± 0.15	-0.86 ± 0.10	–	8.34 ± 0.21	–	1.16	303
46	0.44 ± 0.10	-1.87 ± 0.15	2.66 ± 0.15	–	–	1.28	141
49	0.24 ± 0.05	-1.67 ± 0.18	2.37 ± 0.18	–	–	1.53	<10
36	5.78 ± 1.28	–	–	–	–	1.57	<10
37	7.09 ± 1.56	-1.92 ± 0.62	1.95 ± 0.62	–		1.97	<10
41	8.26 ± 1.82	-1.74 ± 0.64	2.00 ± 0.64	–	–	1.25	174
59	3.83 ± 0.85	-1.93 ± 0.09	2.75 ± 0.09	–	–	1.44	<10

[a]Projected galactocentric distance, corrected according to the method of Scarano et al. (2008).
[b]Oxygen abundances estimated using the N2 calibrator proposed by Marino et al. (2013), which is valid in the range $-1.6 < N2 < -0.2$.
[c]Oxygen abundances estimated using the O3N2 calibrator proposed by Marino et al. (2013), which is valid in the range $-1.1 < O3N2 < 1.7$.
[d]Ratio between emission lines [S II] λ6717 and [S II] λ6731.

Table 5. Luminosities and SFRs for NGC 4656 and NGC 4656UV.

Source	$L_{H\alpha}^{a,b}$ ($\times 10^{40}$erg s^{-1})	$SFR_{H\alpha}^{b,c}$ ($M_\odot$ yr^{-1})
NGC 4656UV	0.04 ± 0.02	0.003 ± 0.001
NGC 4656 A	0.66 ± 0.29	0.053 ± 0.023
NGC 4656 B	0.37 ± 0.16	0.030 ± 0.013
NGC 4656 C	0.14 ± 0.06	0.011 ± 0.005
NGC 4656 whole	1.18 ± 0.51	0.094 ± 0.040

[a]Value estimated in this work using the integrated Hα emission flux.
[b]The assumed distance is 5.1 Mpc (Sorce et al. 2014).
[c]Value estimated in this work using Kennicutt's (1998) formula.

developed by Boulesteix (1993). These curves are constructed from the velocity fields obtained from the FP data, by taking into account the points located inside a given angular sector from the major axis. On this way, we avoid the inclusion of points near the minor axis that show a large dispersion in the computed RC. To estimate the values of velocity and radius, we considered crowns with a width of 25 pixels, and we obtained a rotational velocity and average radius within each crown. For NGC 4656, we considered an angular sector of ±15° from the major axis. To compute the RCs is necessary to adjust some parameters: coordinates of the rotation centre, systemic velocity, position angle of the major axis and inclination of the disc of the galaxy. Since NGC 4656 does not present a clear nucleus, we have adopted as the rotation centre, the point that provided us the most symmetric RC. The systemic velocity was obtained once the optimal superposition between both sides of the RC (approaching and receding sides) was found. The position angle is given counter-clockwise from the north. Due to the irregular shape of the galaxy and its disturbed velocity field, it is not relevant to compute the kinematical inclination of the disc of NGC 4656 (with respect to the plane of the sky); so we have taken different values from literature (Stayton et al. 1983; Schechtman-Rook & Hess 2012). The final parameters used in the RC that best fits to NGC 4656 are shown in Table 7.

4.2 Position–velocity diagrams

The classical method for fitting RCs (see Section 4.1) works properly for low inclination galaxies; however for highly inclined galaxies, as the case of NGC 4656, obtaining RCs through this method is not reliable, since it can lead to large underestimates of the rotation velocities. This is mainly due to the fact that the shape of a profile is obtained from the integration along the line of sight of a large portion of the disc, for which it is necessary to make some corrections to the estimated velocities (Rosado et al. 2013). For this reason, we have built position–velocity (PV) diagrams that allow obtaining a more reliable RC and measurement of the rotation velocity to systems with high inclination.

In this work, the creation of the PV diagrams was done using the code FLUXER.[1] For NGC 4656, we made a mosaic with the six data cubes wavelength calibrated, finally forming a single large cube for the whole galaxy (with a total FoV of 5.8 arcmin×5.8 arcmin). Subsequently, the spectral extraction of the data cube was performed from a slit aligned along the major axis of the system, considering a PA of 40° and a slit width of 2.5 arcsec. Finally, the PV diagram was built directly from graphical interface of FLUXER, which is shown in Fig. 17. The construction of the RC was done from an envelope of the PV diagram, as is explained in detail in Section 5.6.3.

[1]Package for data cubes in IDL, written by Christof Iserlohe. http://www.caserlohe.de/fluxer/fluxer.html

Table 6. SFRs for NGC 4656 and NGC 4656UV.

Source	$SFR^{a,b}_{H\alpha}$	$SFR^{b,c}_{FUV}$	$SFR^{a,d}_{H\alpha}$ $M_\odot yr^{-1}$	$SFR^{d,e}_{FIR}$	$SFR^{a,f}_{H\alpha}$	$SFR^{f,g}_{H\alpha}$
NGC 4656UV	0.006 ± 0.001	0.027 ± 0.001	–	–	–	–
NGC 4656	0.186 ± 0.042	0.666 ± 0.030	0.28	0.23	0.27	0.54

Notes: Values presented on this table has not been corrected by extinction.
[a]Value estimated in this work using the Kennicutt (1998) recipe, based on $L_{H\alpha}$.
[b]It has been considered a distance of 7.2 Mpc (Seth, Dalcanton & de Jong 2005) to both systems.
[c]Value estimated by Schechtman-Rook & Hess (2012), based on L_{FUV}.
[d]It has been considered a distance of 8.8 Mpc (Pilyugin et al. 2008) to both systems.
[e]Value estimated by Pilyugin et al. (2008), based on L_{FIR}.
[f]It has been considered a distance of 8.7 Mpc (Mould et al. 2000) to both systems.
[g]Value estimated by Mapelli et al. (2010), based on $L_{H\alpha}$.

Table 7. Parameters for the rotation curve of NGC 4656.

Parameter	Value
Rotation centre[a]	RA $12^h43^m52^s.893$
	Dec. $32^d08^m54^s.56$
Inclination[b]	82°
PA[c]	40°
Systemic velocity[a]	652 km s^{-1}
Maximum rotational velocity[a]	83 km s^{-1}

[a]Values estimated in this work.
[b]Value extracted from Stayton et al. (1983).
[c]Value extracted from Schechtman-Rook & Hess (2012).

Table 8. The fitted parameters of the kinematic model.

Parameter	Values
V_0	64 ± 41 km s^{-1}
c_0	12.1 ± 1.3 kpc
p	1.0 ± 0.1
v_s	658 ± 1 km s^{-1}
ψ_0	$47.5° \pm 0.4°$
R_{ra}	12:43:48.823
R_{dec}	+32:08:32.88
χ^2_{red}	11.9
$M_{dyn}(R = 12.1\,\text{kpc})$	$6.8^{1.8}_{-0.6} \times 10^9\,M_\odot$

4.3 Velocity field modelling

Considering the complex nature of NGC 4656, we have performed a simple phenomenological model of circular orbits in a plane, following the recipes given by Bertola et al. (1991), we consider the following parametrical axisymmetric rotation curve

$$V_{rot}(r) = \frac{V_0\, r}{(r^2 + c_0^2)^{\frac{p}{2}}}, \tag{2}$$

where r is the radius on galaxy plane, V_0 is related to the amplitude of the rotation curve, c_0 is a concentration parameter. The parameter p defines the form of the rotation curve, varying in the range between 1 (logarithm potential) and 1.5 (Plummer potential, which is a Keplerian-like potential), which is the expected range of values for galaxies. Using the relations linking the velocities in the sky and galaxy planes (Warner, Wright & Baldwin 1973; van der Kruit & Allen 1978), the line-of-sight velocity model on sky plane, $V_{mod}(R, \psi)$, can be written as

$$V_{mod}(R,\psi) = V_s + \frac{V_0\, R\cos(\psi-\psi_0)\sin(i)\cos^p(i)}{\{R^2[\sin^2(\psi-\psi_0)+\cos^2(i)\cos^2(\psi-\psi_0)]+c_0^2\cos^2(i)\}^{\frac{p}{2}}}, \tag{3}$$

where R and ψ are the radial and angular projected coordinates on sky plane, V_s is the systemic velocity, ψ_0 is the position angle of the line of nodes, i is the disc inclination ($i = 0$ for face-on Tullydisks). Furthermore, there are two implicit parameters: the coordinates of the kinematic centre, R_{cx} and R_{cy}. The parameters V_0 and i are degenerates, and hence the values derived, from the fitting, for them are not reliable. Nevertheless, assuming that the ellipticity of the outermost isophote is due to disc inclination we can fix i breaking up the degeneracy. The value for this parameter was taken from Stayton et al. (1983) who performed a photometry analysis on NGC 4656, they found $i = 82°$ for the galactic disc. The uncertainties associated with barycenter velocity, σ_{V_b}, can be easily derived by doing an error propagation of the barycenter equation, so we found

$$\sigma_{V_b} = \frac{c}{\lambda_b}\sigma_{\lambda_b} = \sqrt{\frac{\sum_{\lambda_i=\lambda_0+3*\sigma}^{\lambda_i=\lambda_0-3*\sigma} I_i^2}{(\sum_{\lambda_i=\lambda_0-3*\sigma}^{\lambda_i=\lambda_0+3*\sigma} I_i)^2}}\sigma_\lambda, \tag{4}$$

where c is light speed, λ_b is the measured barycenter wavelength, σ_{λ_b} is the uncertainty of the barycenter wavelength, I_i is the intensity of pixel i, σ is the measured line dispersion, and $\sigma_\lambda \simeq 27$ km s^{-1} is the spectral dispersion for a resolution $R \sim 11\,000$ at H α. The mean uncertainty overall FoV is $\sigma_{V_b} = 9 \pm 3$ km s^{-1}. We performed the fitting by applying the Levenberg–Marquardt method and taking into account the velocity uncertainties. The parameters fitted of the kinematic model are listed in Table 8.

5 RESULTS

5.1 Ionizing mechanisms of regions

Emission-line intensity ratios are a useful tool for classifying the spectra of extragalactic sources. We have constructed the BPT diagnostic diagram (Baldwin, Phillips & Terlevich 1981) to confirm the excitation mechanism of the regions observed in NGC 4656, which is presented in Fig. 2. This plot shows the [O III]/H β versus [N II]/H α line ratios, where blue dot–dashed and red dashed lines correspond to the limit between star-forming objects and active galactic nuclei (AGNs), as described by Kauffmann et al. (2003) and Kewley et al. (2001), respectively.

It was not possible to include any region of NGC 4656UV because none presented the four emission lines needed to be placed on the diagram. On the other hand, there are also some regions of NGC 4656 that are not in the diagram because their emission lines H β and/or [N II] λ6584 were noisy and difficult to measure (regions #10,

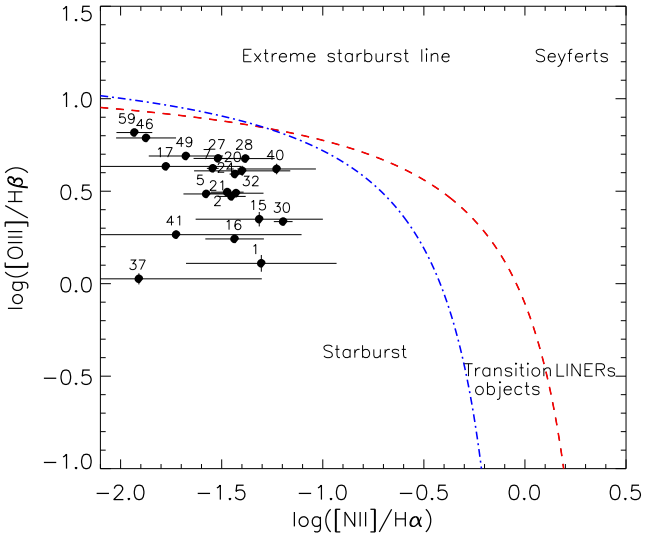

Figure 2. Ionization mechanism diagnostic diagram (Baldwin et al. 1981) for the regions located in NGC 4656. The blue and red dashed line corresponds to the limit between H II regions and AGNs, as described in Kauffmann et al. (2003) and Kewley et al. (2001), respectively.

11, 12, 13, 19, 36, 44, 45, 50, 56, 57, 58, and 60). All the regions that we could locate in the BPT diagram (20 in NGC 4656) are located in the area defined by objects dominated by star formation. Therefore, from the BPT diagram, and taking into account the uncertainties in the fluxes, we conclude that the regions to be analysed correspond to star-forming regions, excluding the AGN activity or ionization by shocks.

5.2 NGC 4656UV

5.2.1 H α emission

Fig. 3 shows a GMOS image in g' band for NGC 4656UV. Circles represent the sources observed with GMOS, blue circles indicate the regions with Hα emission lines at the redshift of NGC 4656UV, and red circles indicate the rest of them that does not present any detected emission line. The green circle represents a region observed with the SDSS. It is important to note that from the 30 regions observed in NGC 4656UV, there are just three of them that exhibit Hα emission (regions #10, #11 and #19). From these three regions only source #19, whose spectrum is presented in Fig. 4, shows the most of emission lines that characterize a H II region (Hβ, [O III] $\lambda\lambda$4959, 5007, Hα, and [S II] $\lambda\lambda$6716, 6731), but the [N II] $\lambda\lambda$6548,6584Å lines were not detected despite the fact that with a resolution R=875, they should be resolved and distinguishable from Hα.

The weak Hα emission of the TDG candidate is confirmed by the monochromatic Hα map obtained from FP data, as shown in Fig. 5 where circles represent regions observed with GMOS under the same colour code than Fig. 3. We can clearly see that in the location where the TDG candidate is supposed to be, there is practically no Hα emission ($<10 \times 10^{-16}$ erg s^{-1} cm^{-1}). The maximum emission is observed beside the region observed by SDSS (green circle), its flux is about 10^{-16} erg s^{-1}cm^{-2} per pixel, which is an order of magnitude higher than in the rest of the system ($\sim 10^{-17}$ erg s^{-1} cm^{-2} per pixel). Due to this weak emission in NGC 4656UV, it was not possible to study its kinematics; however, it was possible to estimate its oxygen abundance (see Section 5.2.2) and SFR (see Section 5.5).

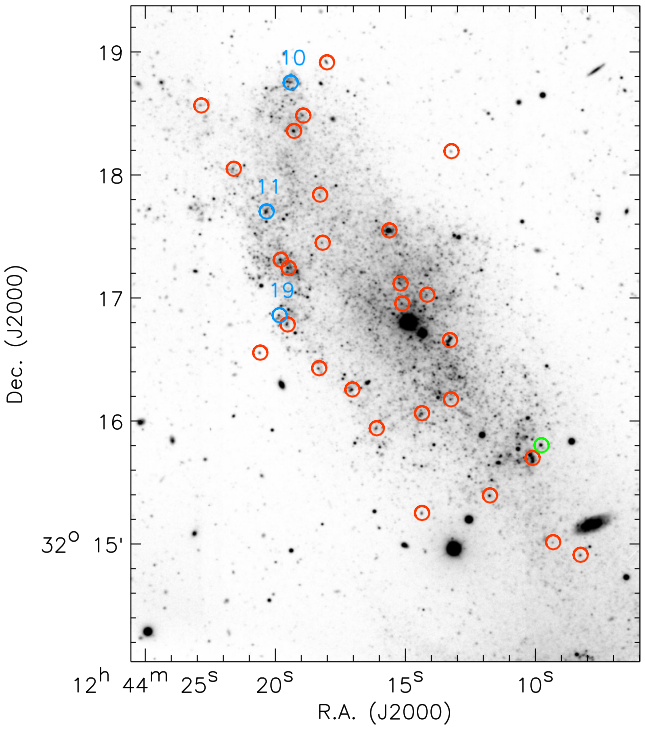

Figure 3. Gemini/GMOS image in g' filter for NGC 4656UV. Red and blue circles represent regions observed. Blue circles represent the regions that have nebular emission lines, and the red ones the regions that do not contain Hα emission. Green circle represents a region with Sloan Digital Sky Survey (SDSS) spectrum.

5.2.2 Oxygen abundance

We have estimated the oxygen abundance for NGC 4656UV from region #11 once its spectrum was binned. We resized the bin between each element of the wavelength axis, decreasing it to half its original size through neighbourhood averaging. The resulting spectrum is shown in Fig. 6. We have obtained an oxygen abundance of 12+log(O/H) $\sim 8.03 \pm 0.20$, through the N2 calibrator (Marino et al. 2013). With the same calibrator, we have also calculated the oxygen abundance for another region of NGC 4656UV observed by SDDS (Fig. 3, green circle), considering the fluxes tabulated in the SDSS DR12 data base, and we obtained a value of $12 + \log(O/H) \sim 8.34 \pm 0.20$. Both oxygen abundances corresponding to different zones of the system are similar, considering the uncertainties in the fluxes and in the Marino et al. (2013) calibrations.

5.3 NGC 4656

5.3.1 H α emission

The Hα monochromatic map for NGC 4656 is shown in Fig. 7. The most intense Hα emission is concentrated in the north-east part of the galaxy, region which is dominated by H II regions surrounded by diffuse emission. These H II regions have a size of the order of hundreds of parsecs ($\sim$150–650 pc). As we move towards the south-west, the number of H II regions decreases and diffuse emission predominates. These results are consistent with what is shown by the GMOS spectra.

On the north-east edge of NGC 4656, there is a feature which gives the galaxy a 'hockey stick' appearance (Schechtman-Rook & Hess 2012) also known as NGC 4657. In order to determine whether

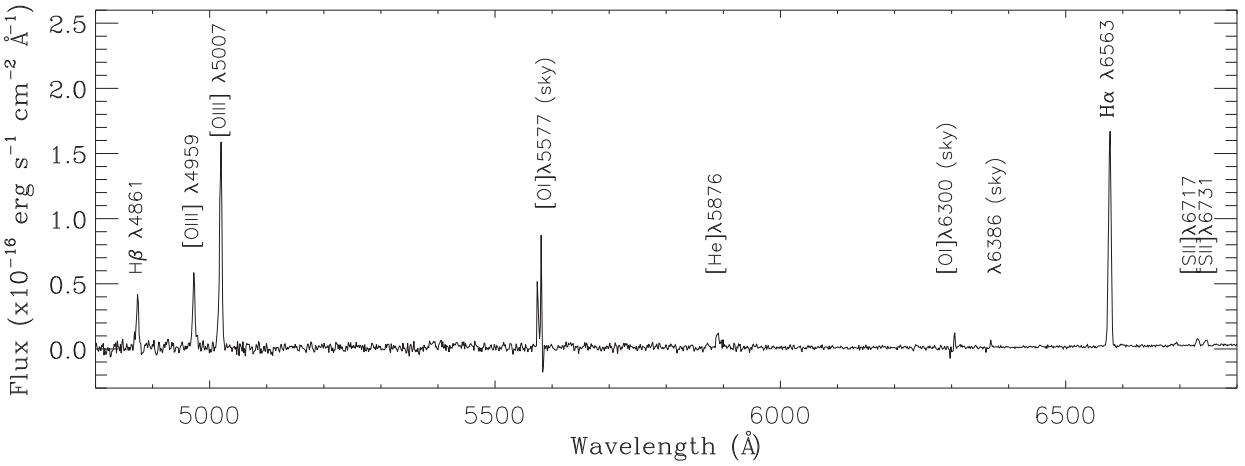

Figure 4. Spectrum of region #19 located in NGC 4656UV, flux calibrated, and corrected by extinction. The main emission lines found are labelled.

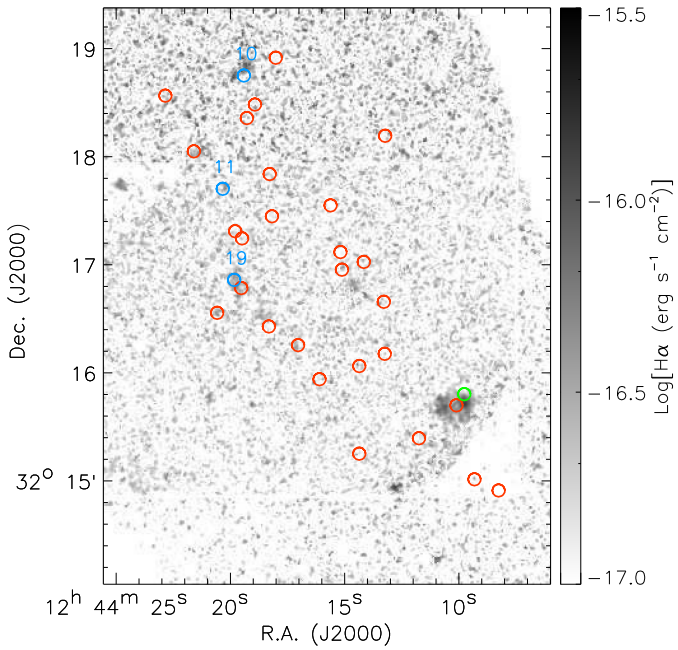

Figure 5. Monochromatic Hα emission map for NGC 4656UV. The circles represent GMOS regions under the same colour code of Fig. 3. The Hα intensity is shown in logarithmic scale.

the NGC 4656 system is a single-disturbed galaxy or two galaxies at some stage of interaction (NGC 4656/4657), we analysed the Hα emission profiles in the connecting area of the two possible galaxies. This area is highlighted in the left-hand panel of Fig. 8 through a red square. The Hα profiles corresponding to this zone are presented in the central and right-hand panels. In the central panel, the Hα profiles have been normalized to the size of the box and in the right-hand panel the same profiles have been normalized to the brightest profile. The profiles in this region are presented as asymmetrical, wide and some with clear multiple peaks of emission. Wide and asymmetric profiles may correspond to lines formed by several components, which cannot be resolved because the spectral resolution is not high enough ($R \sim 11\,000$). Double profiles can be due to star formation in one single galaxy, for example to the presence of an expanding bubble, or can be due to a merging of two systems, where a profile superposition along the line of sight is observed. This kind of analysis has been performed by Amram et al. (2007) using FP data, who concluded that the A+C system in HCG 31 is in an early stage of merging, based on the presence of double profiles of the Hα line in the region that connects components A and C. However, in our case, the most disturbed profiles that can be seen in the area have a very low emission ($<1 \times 10^{-17}$ erg s^{-1} cm^{-2}), as presented in the right-hand panel of Fig. 8. Therefore, these profiles do not show clear evidence indicating the overlapping between two galaxies. The symmetric shape of the intense Hα profiles in the studied area does not suggest the presence of multiple intense components, which could suggest the presence of overlapping profiles and therefore, galaxies in process of merger.

5.3.2 *Oxygen abundances and its distribution*

Oxygen abundance estimates are listed in Table 4. Given the spectral coverage of the observations and the valid range of the calibrators, most of the presented values were obtained through the N2 method.

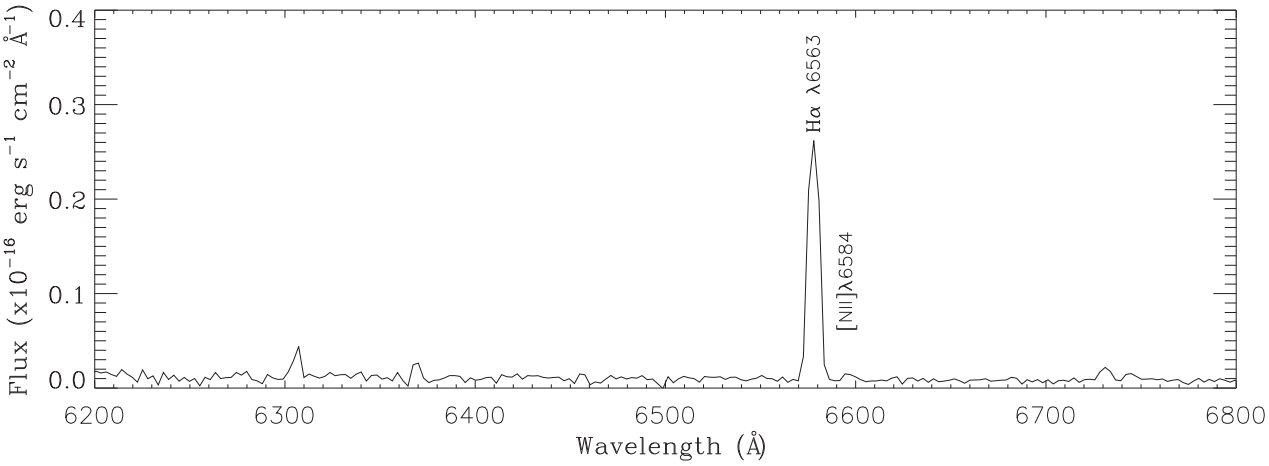

Figure 6. Flux calibrated spectrum of region #11 located in NGC 4656UV, showing the H α emission line.

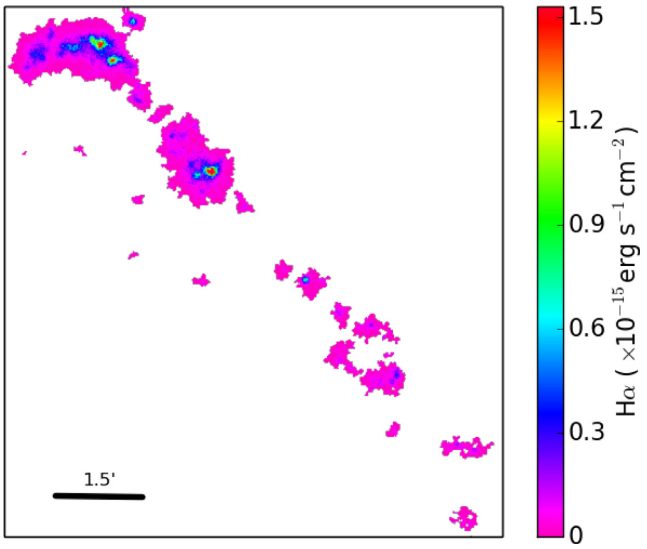

Figure 7. H α monochromatic map for NGC 4656. The colour bar represents the flux in physical units.

Then, the following analysis concerning oxygen abundances refer to the N2 estimates. We found oxygen abundances ranging between 12 + log(O/H) = 8.03 (regions #5 and #7, outwards) and 12 + log(O/H) = 8.34 (region #44, near the centre). The average chemical abundance for NGC 4656 is 12 + log(O/H) = 8.10 ± 0.20.

Fig. 9 shows the oxygen abundance distribution in NGC 4656. On the top panel, blue dots represent the oxygen abundances obtained for regions located at the north-east region of the galactic centre, with their respective identification number (see Fig. 1). The red dots represent the sources observed at the south-west region of NGC 4656. All these sources have N2 indexes out of the valid range of this calibrator. It suggests that these sources have abundances lower than 12 + log(O/H) ∼ 8, which is indicated with red arrows in Fig. 9. From the top panel of Fig. 9, we can note that the metal distribution along NGC 4656 is not symmetric with respect to its centre, with oxygen abundances lower than 12 + log(O/H) ∼ 8 in the south-west sector, and greater than this value in the north-east sector.

The bottom panel of Fig. 9 corresponds to the oxygen abundance distribution obtained for the north-east part of NGC 4656 (blue points in the upper panel), where the solid blue line represents a linear fit applied to the data that has been obtained using the IDL routine MPFITEXY (Williams, Bureau & Cappellari 2010), which considers the uncertainties in both axis. As a comparison, on this plot, we have included the oxygen abundances estimates (N2 method) that we have derived from the emission line fluxes published by Zasov et al. (2017) for this system, and whose distances were re-calculated by us by following the method described in Section 3.3 (we note that Zasov et al. 2017 published oxygen abundances derived from IZI and S methods). These values are represented by green points and the green dashed line shown a linear fit on the data. In addition, on this plot we have included the oxygen distribution for NGC 55, which is a nearby galaxy that displays tidal features and similar characteristics than NGC 4656 (NGC 55 is located at 2.34 Mpc, with a total mass of 2.0 × 10^{10} $M_\odot$ and R_{25} = 11 kpc; Westmeier, Koribalski & Braun 2013; Kudritzki et al. 2016). In order to analyse its oxygen distribution, we used the abundances that were recently published by Magrini, Gonçalves & Vajgel (2017), who used the N2 calibrator proposed by Marino et al. (2013). Finally, projected distances for this system were re-calculated by using the positions given by Magrini et al. (2017) and the method described in Section 3.3. Then, the gradient for NGC 55 is represented by magenta asterisks and a dash–dotted magenta line.

In the case of our measurements for NGC 4656, we found a zero-point of 12 + log(O/H) = 8.19 ± 0.12 and a slope of β = −0.027 ± 0.029 dex kpc^{-1} for the north-east sector of the galaxy, indicating an approximately homogeneous oxygen abundance distribution compared to isolated spiral galaxies, which could display a typical gradient of ∼0.072 dex kpc $^{-1}$ (Zaritsky et al. 1994). It should be noted that the value of β found for NGC 4656 must be taken with caution due to the tidal morphology that it presents. In addition, we found a good agreement between our estimates and the oxygen distribution derived from the fluxes measured by Zasov et al. (2017) (average 12 + log(O/H) ∼ 8.13, slope −0.023 dex kpc^{-1}). This agreement even exists when we compared our measurements (N2 method) with respect to the values obtained by Zasov et al. (2017) through the theoretical IZI method (average 12 + log(O/H) ∼ 8.18, β = −0.03 dex kpc^{-1}). The oxygen distribution obtained in this work also agrees with the gradient obtained by Pilyugin, Grebel & Kniazev (2014) (gradient –0.03 dex kpc^{-1}) following the C method (Pilyugin, Grebel & Mattsson 2012).

On the other hand, unlike the gradient reported in this paper for NGC 4656, the radial metallicity gradient for NGC 55 has a positive slope (+0.011 dex kpc $^{-1}$). Despite this difference, both galaxies

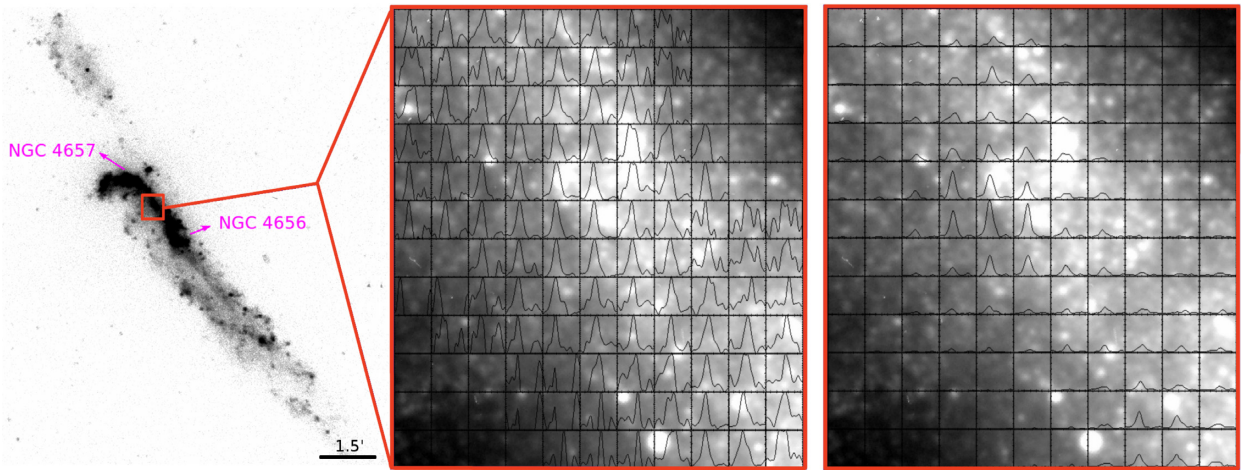

Figure 8. Left: Image in the FUV band of NGC 4656/4657, observed with *GALEX*. The regions that have been designated by some authors as NGC 4657 (north-east sector of the system) and NGC 4656 (south-west sector of the system) are indicated with arrows. The red square corresponds to the area whose profiles are shown in the following panels. Centre: H α profiles obtained after doing a *binning* of 6 × 6 pixels. Each box that contains each profile has dimensions of ∼4.1 arcsec × 4.1 arcsec (∼100 × 100 pc^2). The size of the total region shown is ∼50 arcsec ×45 arcsec (∼1.2 × 1.0 kpc^2). Each profile is normalized to the size of each box. The background image was observed by GMOS in the g' band. Right: H α profiles equivalent to those shown in the left-hand panel. The difference is that in this case the profiles are normalized to the brightest profile shown in this area (∼3.0 × 10^{-17}erg s^{-1}cm^{-2}). The background image is the same as shown in the left-hand panel.

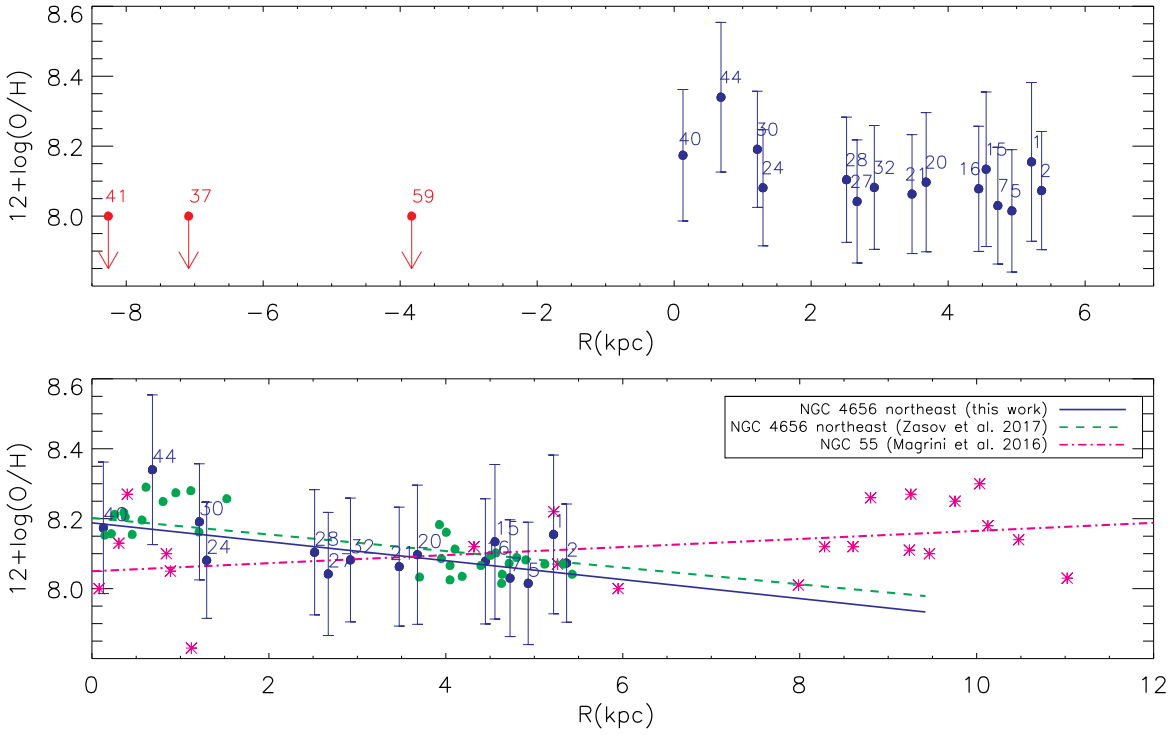

Figure 9. Top panel: Blue dots show the oxygen abundance values obtained for the regions located at the north-east of NGC 4656, with the N2 calibrator (Marino et al. 2013). Red points represent the values for regions located at the south-west of NGC 4656 that have N2 index out of range; therefore, their metallicities are less than 8.0. The latter is represented by red arrows. Bottom panel: Top panel zoom. Blue line represents the metallicity gradient for NGC 4656 regions obtained in this work. The green dashed line represents the oxygen abundance gradient estimated with the N2 calibrator (Marino et al. 2013) for the NGC 4656 regions obtained by Zasov et al. (2017) (green circles). For comparison, the dot–dashed magenta line represents the oxygen abundance gradient estimated with the N2 calibrator (Marino et al. 2013) for the NGC 55 regions obtained by Magrini et al. (2017) (asterisks magenta).

show flat oxygen abundance gradients considering the uncertainties. We can note, furthermore, that both NGC 4656 and NGC 55 reach large radial distances ($\gtrsim$6 kpc and $\gtrsim$11 kpc, respectively) considering their low masses, being that in general irregular dwarf galaxies (10^8–10^{10}M$_\odot$) have diameters between 1 and 10 kpc (Matteucci 2012). For the case of NGC 4656, the furthest galactocentric projected distance calculated in this work is ∼7 kpc (see Table 3), which is very interesting considering that its effective radius is only ∼1 kpc

(Nilson 1973). This fact indicates that the gas flows can produce a mixture of metals and the redistribution of them reaching large distances (Bresolin & Kennicutt 2015), showing how powerful the effect of an interaction in the gas mixture can be.

5.3.3 Electron densities

Emission line ratios (RS2) and electron densities for the H II regions located in NGC 4656, are presented in the penultimate and last column of Table 4, respectively.

We found that 15 sources have an RS2 index that is lower than the theoretical limit (RS2 = 1.43 for a T_e = 10 000 K; Osterbrock & Ferland 2006). For these sources, it was possible to estimate the electron densities, which range between $16 < N_e < 304\,cm^{-3}$, with an average of $N_e = 128$. On the other hand, seven regions present an RS2 value greater than 1.43. In this case, it can be assumed that N_e is lower than $10\,cm^{-3}$; however, the estimation of the electron density becomes uncertain (López-Hernández et al. 2013). Several authors have faced this same situation, using different kind of data (Kennicutt, Keel & Blaha 1989; Zaritsky et al. 1994; Bresolin et al. 2005; López-Hernández et al. 2013). For example, Kennicutt et al. (1989), through long-slit spectra, found that numerous H II regions in spiral galaxies have an RS2 greater than the theoretical limit. On the other hand, using integral field spectroscopy (IFS), López-Hernández et al. (2013) found a similar behaviour for sulfur lines in a sample of H II regions in M33.

In summary, we find that the H II regions belonging to NGC 4656 present electron densities of the order of $N_e \sim 10$–$300\,cm^{-3}$, which is consistent with the typical range found for other extragalactic H II regions, which have typical densities of $N_e \leq 500\,cm^{-3}$. Indeed, 13 sources (of a total of 22) present values of N_e that are in the range estimated by Krabbe et al. (2014) for H II regions located in interacting galaxies ($N_e = 24$–$532\,cm^{-3}$), which is consistent with the stage of the system NGC 4656.

5.4 Mass–metallicity relation

A useful tool for understanding the formation and evolution of galaxies is the mass–metallicity relation (MZR). Using data from the SDSS, several authors have confirmed that there is a correlation between the stellar mass of galaxies and metallicity in gas phase (Tremonti et al. 2004; Kewley & Ellison 2008; Salim et al. 2014). Interestingly, some authors (e.g. Weilbacher et al. 2003) have shown that TDG candidates do not follow the MZR defined by primordial dwarf galaxies. Therefore, by studying the location of NGC 4656/4656UV in the MZR diagram can given us important clues about the origin of these galaxies.

In order to examine location of NGC 4656 and NGC 4656UV in the MZR, we have considered as a control sample the study carried out by Jimmy et al. (2015), who analyse the low-mass regime of this relation. Given that Jimmy et al. (2015) derived oxygen abundances from the N2 calibration proposed by Denicoló, Terlevich & Terlevich (2002), we have recomputed the nebular abundances using this calibrator, yielding 12 + log(O/H) = 8.07 and 12 + log(O/H) = 8.26 for NGC 4656 and NGC 4656UV, respectively.

The stellar mass for NGC 4656 was derived from its near-IR emission (*H* and *K* bands; Schechtman-Rook & Hess 2012) and from an averaged M/L ratio derived from nine different colours[2] (see Bell et al. 2003). We obtained $M/L_H = 0.72$, $M/L_K = 0.66$, which translate into an average stellar mass of $M_* = 8.57 \times 10^8 M_\odot$. In the case of NGC 4656UV, the stellar mass was derived by using its g'-band luminosity, given the lack of good photometry in the near IR. In this case, we obtain a stellar mass of $M_* = 5.46 \times 10^7 M_\odot$.

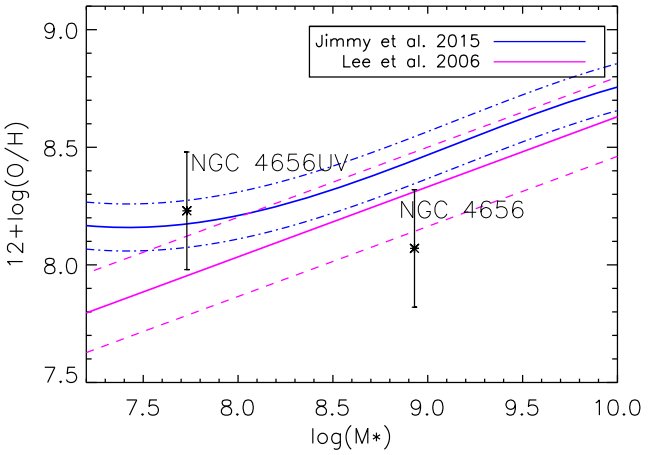

Figure 10. MZR for NGC 4656 and NGC 4656UV. The blue solid line represents the MZR estimated by Jimmy et al. (2015) for normal dwarf galaxies, the dot–dashed line represents the error of the fitting at 1σ. The solid magenta line represents the MZR estimated by Lee et al. (2006) for dwarf galaxies with star formation; the dotted line represents the error of the fitting at 1σ.

In Fig. 10, we show the MZR studied by Jimmy et al. (2015) (blue lines), where we have included the data for NGC 4656 and NGC 4656UV (black asterisks). The error bars in the chemical abundances represent an uncertainty of 0.25 dex, which arises from the scatter in the calibration [uncertainties updated by Pérez-Montero & Díaz (2005) based on the calibration proposed by Denicoló et al. (2002)]. In addition, magenta lines represent the MZR found by Lee et al. (2006) for a sample of dwarf irregular galaxies, where abundances were obtained through the direct method. As shown in Fig. 10, NGC 4656UV follows the relation defined by normal dwarf galaxies (Jimmy et al. 2015), contrary which is expected for TDGs. Indeed, for newly formed TDGs, in which the *in situ* production of metals is insignificant compared to the metals coming from the interacting progenitor galaxies, it is expected that they do not follow an MZR (Duc & Mirabel 1998). In this context, this result suggests that the TDG candidate would not have a tidal origin. In the case of NGC 4656, we found that this object lies below the relation proposed by Jimmy et al. (2015), with an abundance very similar to the value found for NGC 4656UV.

5.5 Star formation rates from H α luminosity

In order to determine how the SFR varies along NGC 4656, SFRs were estimated in three main sectors, namely A, B, and C, and which are shown in Fig. 11. The selection of these boxes was made through visual inspection of the monochromatic map of NGC 4656 based on its morphology. We estimated the values of $SFR_{H\alpha} = 0.053 \pm 0.023\,M_\odot\,yr^{-1}$,

[2]The nine colours used were $(g' - r')$, $(u' - g')$, $(u' - r')$, $(u' - i')$, $(u' - z')$, $(g' - i')$, $(g' - z')$, $(r' - i')$, and $(r' - z')$. These were estimated considering the fluxes listed in Schechtman-Rook & Hess (2012, table 2).

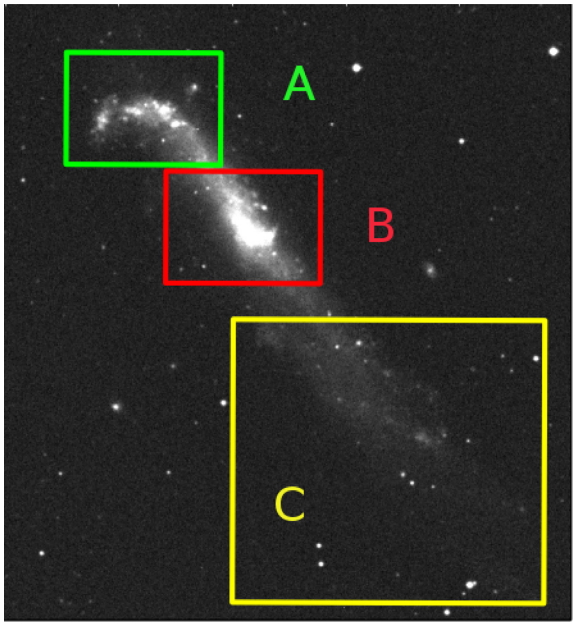

Figure 11. Digital Sky Survey *R*-band image for NGC 4656. Green (2.9 arcmin×2.0 arcmin), red (2.9 arcmin×2.0 arcmin), and yellow (5.8 arcmin×5.3 arcmin) boxes represent the regions that were used to compare SFRs in NGC 4656.

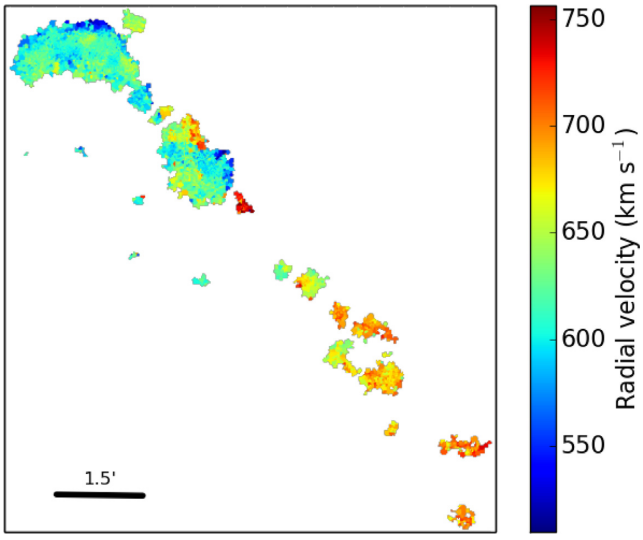

Figure 12. Radial velocity map for NGC 4656. The colour bar represents the velocity units of km s^{-1}.

$SFR_{H\alpha} = 0.030 \pm 0.013\,M_\odot\,yr^{-1}$, and $SFR_{H\alpha} = 0.011 \pm 0.050\,M_\odot\,yr^{-1}$ for the A, B, and C regions, respectively, and whose values are summarized in Table 5.

Considering the large uncertainties, we note that region A displays a larger SFR than region C (despite the different covered area, see Fig. 11), indicating that the north-east region of NGC 4656 is actively forming stars. In the case of NGC 4656 as a whole, we obtained an $SFR_{H\alpha} = 0.094 \pm 0.040\,M_\odot\,yr^{-1}$. This value of $SFR_{H\alpha}$ locates NGC 4656 in the star-forming sequence in the M_*–$SFR_{H\alpha}$ plane (considering the uncertainties), according to the relation estimated by Zahid et al. (2012)[3] (who consider a mass range of $\log(M_*) \sim 8.5$–10.4). For the TDG candidate, we obtained a luminosity of $L_{H\alpha} = 4.00 \pm 2.00 \times 10^{38}$ erg s^{-1} and $SFR_{H\alpha} = 0.003 \pm 0.001\,M_\odot\,yr^{-1}$, placing this object in the star-forming sequence defined for dwarf galaxies with low-surface brightness (LSB; McGaugh, Schombert & Lelli 2017).

In order to compare our results with those obtained in literature, we have also estimated the luminosities and SFRs considering the distances assumed by the different authors (Pilyugin, Izotova & Sholudchenko 2008; Mapelli et al. 2010; Schechtman-Rook & Hess 2012). The results are presented in Table 6. Using a distance of 7.2 ± 0.8 Mpc (Seth, Dalcanton & de Jong 2005), which was adopted by Schechtman-Rook & Hess (2012), we obtained the value of $SFR_{H\alpha} = 0.186\,M_\odot\,yr^{-1}$ for NGC 4656 and $SFR_{H\alpha} = 0.006\,M_\odot\,yr^{-1}$ for NGC 4656UV as a whole. Based on the FUV luminosity, Schechtman-Rook & Hess (2012) found the values of $SFR_{FUV} = 0.666\,M_\odot\,yr^{-1}$ and $SFR_{FUV} = 0.027\,M_\odot\,yr^{-1}$ for NGC 4656 and NGC 4656UV, respectively. For both cases, we found discrepancies between these last values and those calculated in this work. We can note that for NGC 4656 the $SFR_{H\alpha}$ is ∼3 times lower than the SFR_{FUV} obtained by Schechtman-Rook & Hess (2012), and for NGC 4656UV the $SFR_{H\alpha}$ is ∼4 times smaller than the SFR_{FUV}. Indeed, previous authors have found a systematic difference between SFRs derived from Hα and UV emission. For example, Lee et al. (2009) found that Hα emission tends to underestimate the total SFR with respect to FUV, in the case of low-luminosity dwarf galaxies. These authors suggest that variations in the initial mass function (IMF) could explain the differences, arguing a possible deficiency of massive ionizing stars in low-mass galaxies. Using a distance of 8.8 Mpc (Pilyugin et al. 2008), we obtained an $SFR_{H\alpha} = 0.28\,M_\odot\,yr^{-1}$ for NGC 4656. Pilyugin et al. (2008) calculated the SFR for NGC 4656 based on the L_{FIR} luminosity, obtaining a value of $SFR_{FIR} = 0.23\,M_\odot\,yr^{-1}$. Comparing both SFRs, we can see that both results are similar. Considering a distance of 8.7 Mpc (Mould et al. 2000), value considered by Mapelli et al. (2010), we obtained the value of $SFR_{H\alpha} = 0.27\,M_\odot\,yr^{-1}$ for NGC 4656. Based also on $L_{H\alpha}$ (fluxes extracted from Moustakas & Kennicutt 2006), Mapelli et al. (2010) estimated the value of $SFR_{H\alpha} = 0.54\,M_\odot\,yr^{-1}$. As we can notice, Mapelli et al. (2010) obtained an $SFR_{H\alpha} \sim 2$ times higher than the one estimated in this work. A factor that can affect this discrepancy is the extinction correction, given that the attenuation by dust can cause an underestimation of the intrinsic luminosity of the system. The fluxes used in this paper were not corrected by extinction, on the other hand, the fluxes used by Mapelli et al. (2010) are corrected by Galactic extinction and interstellar absorption. Another relevant factor of great influence to consider, is related to the uncertainties caused by the indirect calibration of the FP Hα maps from the GMOS data (RMSE = 1.32 × 10^{15} erg s^{-1} cm^{-2}, see Section 2.3.2).

5.6 Kinematics

5.6.1 Radial velocity and velocity dispersion

Fig. 12 shows the velocity field along the whole NGC 4656 galaxy. On a large scale, it can be seen that the velocities from the north-east to the south-west range from blue to red respectively (from ∼520 to ∼720 km s^{-1}), which indicates that the global kinematic of the galaxy is still dominated by rotation. This is nevertheless not observed when analysing the field of velocities on a smaller scale. For example, in the north-east, central and southeast areas by

[3]log(SFR)=0.71 log M_*-6.78 (Zahid et al. 2012)

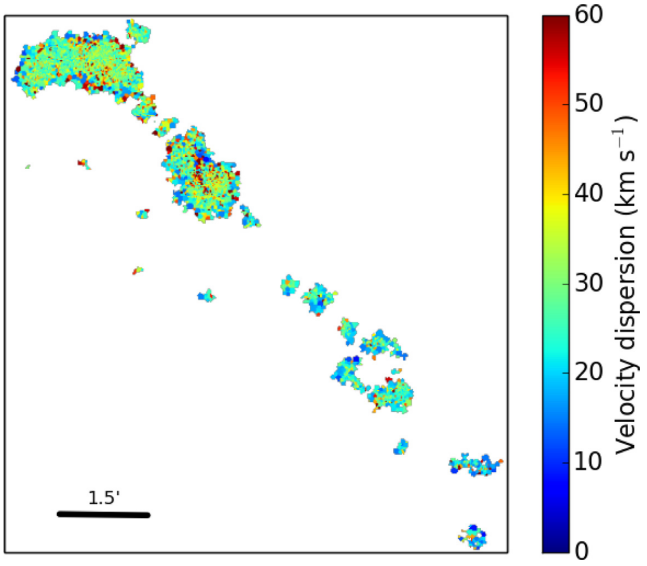

Figure 13. Dispersion velocity map for NGC 4656. The colour bar represents the velocity units of km s^{-1}.

separate, we can see that the velocity field is very disturbed and does not present a well-behaved velocity gradient (see Section 5.6.2).

The velocity range found in this work for the ionized gas (from ∼520 to ∼720 km s^{-1}) is consistent with the velocity range for the H I gas found by Schechtman-Rook & Hess (2012) (from ∼590 to ∼720 km s^{-1}). These authors found the presence of gas that is counterrotating with respect to the disc, in the north-east region of the galaxy centre. In order to determine if the ionized gas presents similar characteristics, we have proceeded to analyse in detail this area considering that our data have better spatial resolution than H I data. For this purpose have been constructed RCs, whose results are presented in Section 5.6.2.

The velocity dispersion map corrected from instrumental broadening for NGC 4656 is presented in Fig. 13. It can be seen that the values of the velocities dispersion throughout the galaxy are fairly uniform ($\sigma \sim 24$–30 km s^{-1}). For nearby dwarf star-forming galaxies, where the velocity dispersion reflects the inner motions of gas in H II regions, a velocity dispersion that does not exceed 30 km s^{-1} is quite typical (Epinat, Amram & Marcelin 2008; Moiseev, Tikhonov & Klypin 2015). For NGC 4656, we have found a flux-weighted average velocity dispersion of $\sim 30 \pm 11$ km s^{-1}, whose uncertainty is represented by the standard deviation. This value is within the range of typical values for dwarf star-forming galaxies. On the other hand, for the upper part of the galaxy, the flux-weighted velocity dispersion is 29 ± 9 km s^{-1}, while for the central part this value is 33 ± 12 km s^{-1} and for the tail 26 ± 12 km s^{-1}.

Non-virial gravitational motions such as ISM turbulence produced by tidal interactions, galaxy mergers, and gas accretion events can influence in the broadening of emission lines that are observed in an integrated way in galaxies (Bournaud et al. 2011; Arribas et al. 2014). For this reason, we also analyse the velocity dispersion in the area that connects the two possible galaxies (NGC 4657 and NGC 4656), which was previously presented in Fig. 8. This region is not dominated by wide profiles (σ greater than 30 km s^{-1}), being the flux-weighted velocity dispersion of ∼27 km s^{-1}. The presence of wide profiles would indicate the presence of multiple components due to a merger process between two galaxies (NGC 4657 and NGC 4656), which would mean that the two systems still have their own kinematic and that they are not totally relaxed. An example is the work done by Amram et al. (2007) for the case of HCG 31, where they find the presence of wide profiles greater than 30 km s^{-1} in the region that connects galaxies A and C, evidence of an ongoing merging.

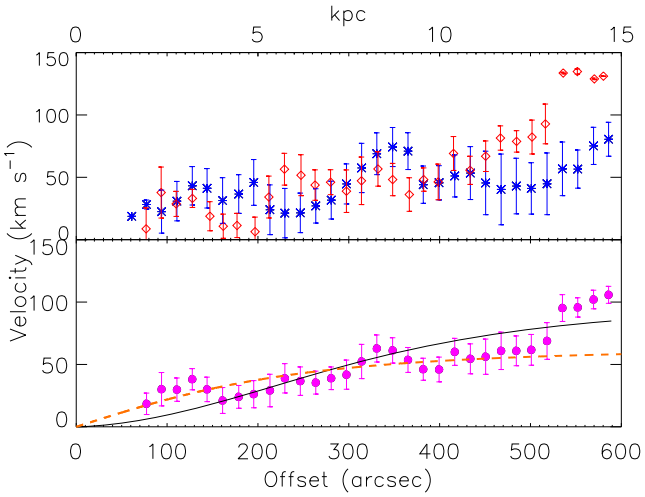

Figure 14. Rotation curves for NGC 4656. Top panel: Curve parameters are PA = 40°, $i = 82°$, and $V_{sys} = 652$ km s^{-1}. Asterisks and diamonds represent the average value of velocities contained in crowns of 25 pixels. Red symbols represent the receding side and blue symbols represent the approaching side of the curve. The associated error bars correspond to the mean deviation. Bottom panel: curve obtained by the average between the approaching and the receding side from the curve presented in the top panel. The continuous black line represents the Zhao function (Kravtsov et al. 1998) fitted to the points. The orange dashed line represents the RC from the best fitting providing a logarithm-like potential (see Section 5.6.4 for more details).

5.6.2 *Rotation curves*

We have derived RCs for the whole galaxy NGC 4656, with different parameters. In both panels of Fig. 14, we present the best RC obtained, whose parameters are listed in Table 7. The inclination and position angle of the major axis were fixed along the radius, given that the line map and velocity field do not indicate the presence of warps or flares, except at the north-east region of this system (where 'NGC 4657' is located). The top panel presents the approaching (blue symbols) and receding (red symbols) sides of the curve. Asterisks and diamonds represent the average value of velocities contained in crowns of 25 pixels. The bottom panel presents the average curve obtained from the approaching and receding sides shown in the top panel. A fit represented by the continuous black line is showed, which corresponds to the Zhao function (Kravtsov et al. 1998). From this model, we obtained that the maximum rotational velocity of the galaxy is 83 km s^{-1}, at a radial distance of 600 arcsec of the kinematic centre.

The nature of the gravitational support of a system in equilibrium is given by the ratio of the maximum circular rotation velocity V_{max} and the local velocity dispersion σ. Due to gravitational perturbation due to interaction with the companion galaxies, NGC 4656 is maybe not a system at equilibrium, so only as a reference we have calculated that ratio. Considering the previously obtained values $V_{max} \sim 83$ km s^{-1} and $\sigma \sim 30$ km s^{-1}, the ratio between both values is $V_{max}/\sigma \gtrsim 2.8$. In this case, we have a high circular velocity compared to velocity dispersion ($V_{max}/\sigma > 1$) which is the signature of a rotation-dominated gravitational support.

In order to investigate if NGC 4657 could be self-gravitating, we zoom its velocity field in the top left-hand panel of Fig. 15. We performed the same analysis on the centre of NGC 4656 (Fig. 15, bottom left-hand panel) that also looks disconnected from the rest of the system. The left-hand panels of Fig. 15 shows that both systems display no clear velocity gradients (a sort of velocity gradients can be seen at very small physical scales), which is insufficient to indicate that NGC 4657 is dominated by circular motion, except of course if the system is almost face-on, which does not seem to be the case. In addition to the low amplitude velocity gradient, the perturbed velocity fields do not allow to compute any reliable RC, considering that in addition the inclination for both system are impossible to evaluate due to their peculiar morphology. As example, the right-hand panel of Fig. 15 shows two construction attempts of the RC for NGC 4657 and the centre of NGC 4656. Those velocity plots show an almost constant radial velocity along the cut and confirm that none of these entities are self-gravitating.

On the other hand, analysing the velocity maps in detail we can notice that there is a small area in the north-east sector of the centre that has a rather large velocity gradient, which could be related a local rotation of gas that can be associated with an independent kinematic underlying a self-gravitating structure. To study this possibility, rotation curves were produced in this area, considering the regions covered by the cone delimited by the two crossed lines in bottom left-hand panel of Fig. 15. As an example, two rotation curves obtained considering two different inclination are presented in Fig. 16. In spite of the different inclination values used, the RC is relevant since a reasonable agreement is obtained between the curves of the approaching and receding sides. We can furthermore consider that this region is rotating with a position angle almost perpendicular to the galaxy as a whole. This is according to the findings of Schechtman-Rook & Hess (2012), who see gas north-east of the centre of the galaxy which is counterrotating with respect to the disc.

5.6.3 *PV diagrams*

The PV diagram for NGC 4656 along the major axis of the galaxy is shown in the upper panel of Fig. 17, where the isocontours represent the intensities at 1, 3, 5, 7, and 9σ above the rms noise of the PV diagram.

Taking into account the broadening of the Hα profiles due to the integration of these along the line of sight, which tends to provide a rotation curve with a solid body shape instead of a more flatten one, at each radius, the line-of-sight velocity is provided by the one with the largest deviation from the systemic velocity, after correction for instrumental broadening and random motions.

We estimated an external limit for the PV diagram from the outer envelope of the PV diagram. This envelope is defined as the isocontour corresponding to 5σ over the rms noise, after making a correction for the average velocity dispersion of the system ($\sim$30 km s^{-1}, see Section 5.6.1), in order to avoid influence of local motions. Similar to the procedure described by Garrido et al. (2005), we fitted a function of Zhao (Kravtsov et al. 1998) that is shown in the lower panel of Fig. 17 (continuous blue line). From this fitting, we compute a function that is flatter and that represents the actual LoS velocity of this almost edge-on galaxy; in addition, we derived the maximum rotation velocity as $V_{\rm max} = V_{R\rm max}/\sin(i)$, where $V_{R\rm max}$ corresponds to the maximum radial velocity of the envelope and i to the inclination (82°, Stayton et al. 1983). Finally, we obtained the value of $V_{\rm max} = 85$ km s^{-1}, which is similar to the one obtained with the rotation curve constructed through the classical method (83 km s^{-1}). Considering this new value, we obtain the same previous ratio of $V_{\rm max}/\sigma \gtrsim 2.8$, which confirms the gravitational support of NGC 4656 is dominated by rotation. It is worth to note that the expected maximum rotational velocity for NGC 4656 from the near infrared Tully–Fisher relation (Torres-Flores et al. 2011) corresponds to 92 ± 18 km s^{-1} (considering an apparent magnitude of 9.1 and a distance modulus of 28.5). This value is fully consistent with our estimates of $V_{\rm max}$ for this system.

5.6.4 *Velocity field model*

Fig. 18 shows the observed velocity field (left-hand panel), the fitted kinematic model (centre panel), and the residual map (right-hand panel). Following Warner et al. (1973) or van der Kruit & Allen (1978), we do not observe any structure in the residual velocity field that could be the consequence of an incorrect determination of the projection parameters (inclination, centre, position angle, systemic velocity). Streaming motion that may occur in such an interacting system are not observed in those maps. Instead, residual velocities are mainly linked to expanding bubble due to star formation events. The best-fitted parameters and their respective uncertainties are given in Table 8, as well as the reduce χ^2 of the fitting. We can see from the residual map that for bulk of points the fit was rather good. In fact, nearly 70 per cent of the profiles have an rms of 13.7 km s^{-1}, which is quite consistent with uncertainties. Most profiles with high residuals are localized in two regions at the west edge-border of the central part of NGC 4656 (compare the zoom of the velocity field at left-bottom panel of Fig. 15 and the residual image of Fig. 18), even the north one is part of counter-rotating zone identified in Section 5.6.2. The kinematic centre given by the fitting is in a good agreement, within the spatial resolution, with that found by Schechtman-Rook & Hess (2012) for H I data (red 'x' at the left-hand panel of Fig. 18). In bottom panel of Fig. 14, we plot the RC of the best-fitting model (orange dashed line) overlaid on average curve between approaching and residing sides. It can be seen that there is a good match between the RC and the observations. The RC reaches its peak around 12.1 $\pm$ 1.3 kpc, becoming flattened from this point. This form of the RC is typical of logarithm-like potentials ($p = 1 \pm 0.1$), as it is expected for a disc galaxy as NGC 4656. We can compute a dynamical mass for NGC 4656, at the radius ($R =$ 12.1 kpc) of the RC peak, $M(R) = \alpha \frac{RV^2(R)}{G}$, where α accounts for the flatness of the disc. By assuming a flat disc model, i.e. $\alpha = 0.6$ (Nordsieck 1973), the estimated value for dynamical mass at this radius is $6.8^{1.8}_{-0.6} \times 10^9$ M$_\odot$. The rotational velocities being quite lower than $\sim$40–60 km s^{-1} up to a large radius of $\sim$12 kpc, it is likely that, in addition to rotation, part of the gravitational support is provided by velocity dispersion. Taking into account that α grows up to 1 when the infinitely flat disc component thicknesses up to a spherical structure, this mass is a lower limit.

6 DISCUSSION

6.1 NGC 4656: one or two entities?

According to Makarov & Karachentsev (2011), NGC 4656 is immersed in a group of galaxies that has 28 members in a harmonic radius of 243 kpc, being NGC 4631 the brightest galaxy. In this environment, it is common for interactions to occur between their members (Bothun 1994).

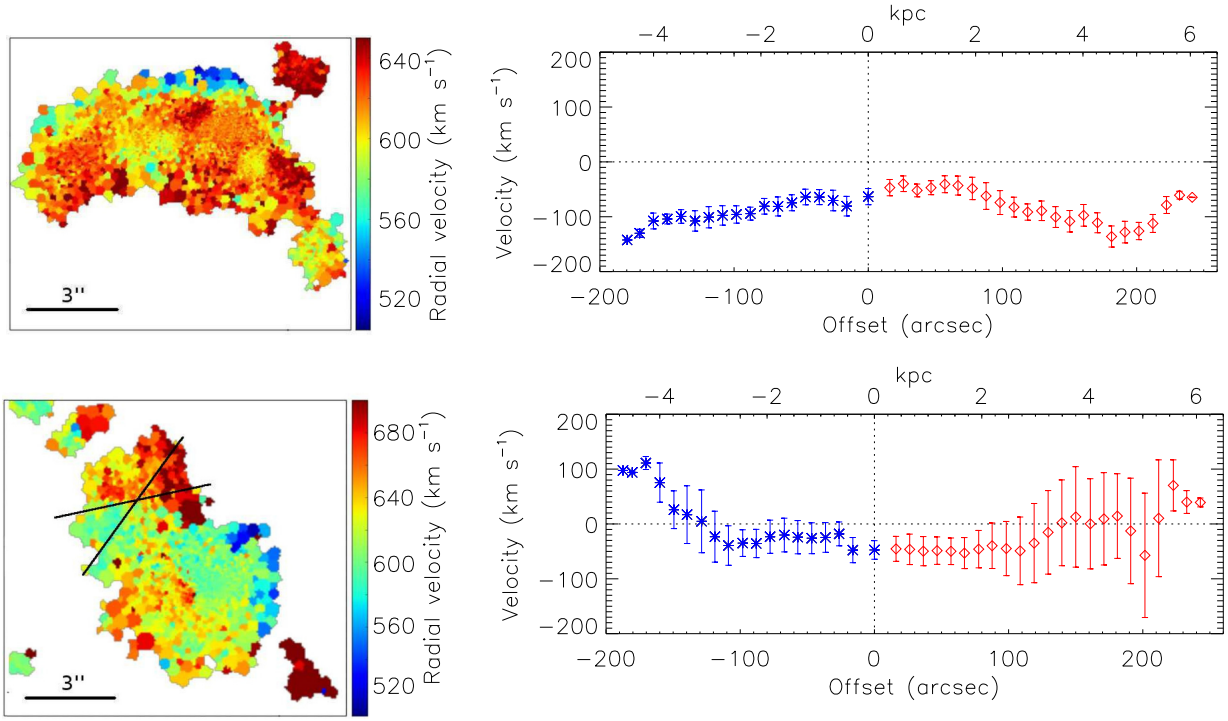

Figure 15. Top left-hand panel: Velocity map for NGC 4657. Top right-hand panel: PV plot for NGC 4657, constructed from the map shown in the top left-hand panel. The parameters used are PA = 70°, $i = 82°$, and Vsyst = 652 km s^{-1}. An angular sector of 20° has been chosen around the major PA. Bottom left-hand panel: Velocity map for the centre of NGC 4656. Two crossed black lines have been superimposed over an area that has a velocity gradient, which represent two cones that contain the points used to make the rotation curves shown in Fig. 16. The intersection between both curves represents the centre used for the curves. Bottom right-hand panel: PV plot for the centre of NGC 4656, constructed from the map shown in the bottom left-hand panel. The parameters used are PA = 35°, $i = 82°$, and Vsyst = 652 km s^{-1}. An angular sector of 30° has been chosen around the major PA.

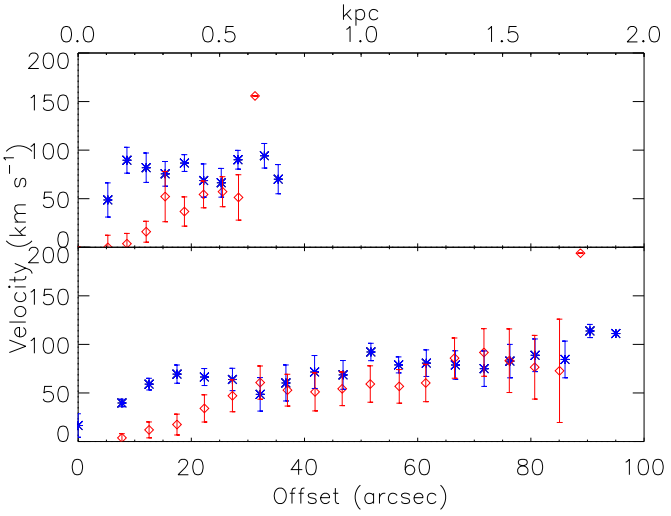

Figure 16. Rotation curves for the counter-rotating zone indicated by the black cones in Fig. 15 bottom left-hand panel. Top panel: The parameters of the curve are PA = 130°, $i = 40°$, and $V_{\rm syst}$ = 645 km s^{-1}. The left-hand panel shows the curve along the entire extension of the region, considering as centre equal to 0 arcsec, while the right-hand panel shows the superposition of both sides of the curve in a single quadrant. Bottom panel: The parameters of the curve are PA = 130°, $i = 80°$, and $V_{\rm syst}$ = 645 km s^{-1}. The left-hand and right-hand panels represent the same as in the top panel.

Some authors considered that NGC 4656 is actually composed by two galaxies: NGC 4657, which would correspond to the north-east extreme of the system, and NGC 4656 that would correspond to the south-west sector, including the optical centre (de Vaucouleurs & de Vaucouleurs 1964; Nilson 1973). For example, according to de Vaucouleurs & de Vaucouleurs (1964), NGC 4656 and NGC 4657 would be in the process of merger, analogous to the antennae, and on the other hand, Nilson (1973) propose that the continuity between both galaxies would be only a projection effect, with NGC 4657 superimposed on NGC 4656.

In this paper, we performed a detailed analysis devoted to determine the nature of the NGC 4656/57 system. Through the con-

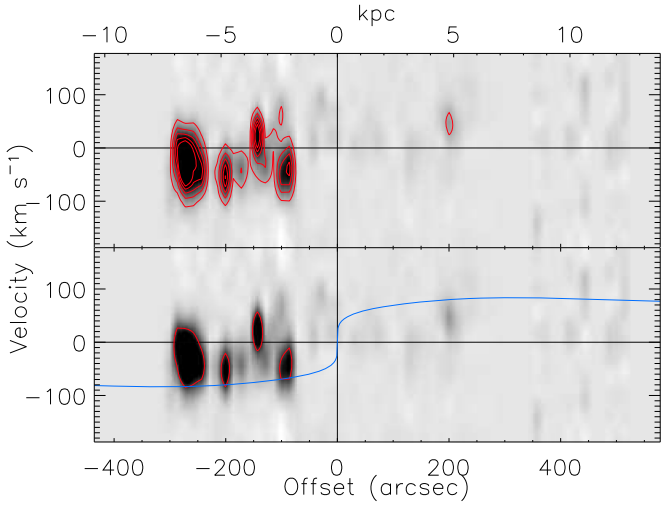

Figure 17. PV diagram for NGC 4656, aligned with the major axis of the system. Top panel: the blue isocontours represent the Hα flux at 1, 3, 5, 7 and 9σ over the rms noise. Bottom panel: The red isocontour represents the envelope defined at 5σ above the rms noise. The continuous blue line represents the Zhao fitting made on the envelope.

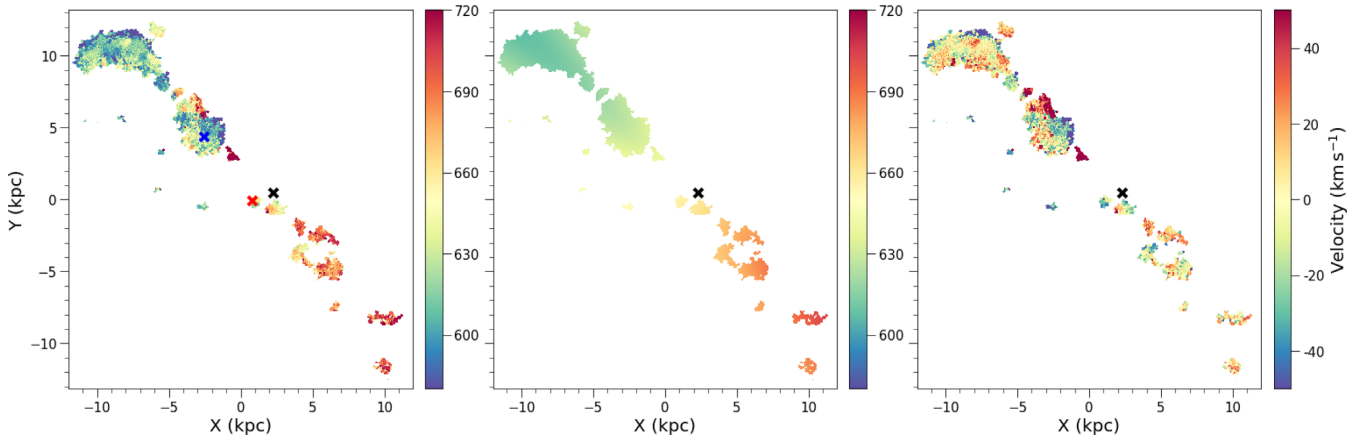

Figure 18. Kinematic model of NGC 4656. Left: observed velocity field in Hα of NGC 4656. Centre: the best model fitted. Right: the residual map of velocities. The photometric centre of the galaxy is marked with the blue 'x', The kinematic centres in Hα and H I (obtained from Schechtman-Rook & Hess 2012) are marked with the black and red 'x', respectively.

struction of rotation curves by the classic method and PV diagrams, we find that NGC 4656 is dominated by rotation ($V_{max}/\sigma \gtrsim 2.8$) on a large scale. The rotation remains predominant but disturbed at smaller scales. Furthermore, as can be seen in Fig. 18 the whole observed velocity field is consistent with the projected phenomenological model that assume only rotation motions in a plane (Bertola et al. 1991). On the other hand, no independent rotations are observed for the north-east and south-west regions of the system, which if observed, could confirm the existence of two individual entities (as suggested by previous authors). We also analysed the Hα profiles in the area that connects the two possible galaxies, since the presence of double-emission profiles could be associated with star-forming processes associated with different galaxies. We found the presence of some asymmetric and double-peaked profiles, however these have a low emission and there is no progressive overlap of the profiles in the whole region, as found by Amram et al. (2007) for the central region of the merging system HCG 31. Therefore, in the case of NGC 4646, these profiles would not indicate a merger between two galaxies, concluding that NGC 4656 is a single-perturbed galaxy.

6.2 Oxygen abundance gradient

The distribution of metals in the discs of spiral galaxies has been studied by several authors (Zaritsky et al. 1994; van Zee et al. 1998; Moustakas et al. 2010; Sánchez et al. 2014), who have found that most of spiral galaxies show clear chemical gradients, where the central regions are most metal rich than the outskirts. On the other hand, numerous observational studies have found that interacting galaxies have flatter gradients and lower nuclear metallicities than isolated galaxies (Kewley et al. 2010; Rupke, Kewley & Chien 2010b; Bresolin, Kennicutt & Ryan-Weber 2012; Rich et al. 2012; Rosa et al. 2014; Torres-Flores et al. 2014; Olave-Rojas et al. 2015). Numerical simulations indicate that this drop in nuclear abundances is produced by gas inflows and gas redistributions along the galactic discs, which also produces a general flattening in the metal distribution (Montuori et al. 2010; Rupke et al. 2010a; Torrey et al. 2012).

For the case of irregular dwarf galaxies, numerous observational studies show that, in general, these galaxies have a low or no oxygen abundance gradient (Hunter & Hoffman 1999; van Zee & Haynes 2006; Croxall et al. 2009). However, Pilyugin, Grebel

& Zinchenko (2015) found that irregular galaxies can also exhibit pronounced oxygen abundance gradients, there being a strong correlation between this radial gradient and the surface brightness profile, in this way galaxies with a flat brightness profile would show a gradient of soft or zero oxygen abundance, and vice versa. These authors indicate that irregular galaxies with a pronounced brightness profile would not be under the influence of a strong radial mixture of gases; on the other hand, irregular dwarf galaxies with a flat brightness profile would be affected by this mixture of gases (e.g. through radial gas flows), resulting in flatter abundance gradients compared to those galaxies with pronounced brightness profiles.

Towards the north-east region of the optical centre of NGC 4656, the oxygen abundance gradient displays a slope of $\beta = -0.027 \pm 0.029$ dex kpc $^{-1}$, which suggests that it is almost flat, considering the uncertainties. In the case of the south-west region of NGC 4656, which is shaped like an extended tail, it was not possible to measure the chemical abundances with the N2 calibrator of Marino et al. (2013), since the H II regions have an N2 index outside the valid range for this calibrator ($-1.6 < \mathrm{N2} < -0.2$), which means that its oxygen abundances have a value less than $12 + \log(\mathrm{O/H}) \sim 8.0$ (see Fig. 9, top panel). Therefore, the distribution of metals across NGC 4656 is not symmetric with respect to its centre. This kind of chemical azimuthal variations are not common, and just a few galaxies have shown features associated with these azimuthal variations (e.g. Ho et al. 2017, 2018). In addition, these chemical disturbances have not been widely studied for interacting galaxies. In this context, the rotation motions play a fundamental role in gas mixing across the galaxy discs (Roy & Kunth 1995). For these reasons, we have estimated the time that NGC 4656 would take to complete an entire rotation. Assuming a rotational velocity of 85 km s^{-1}, we estimate a value of ∼800 Myr. This time is much longer than the time-scale associated with the interaction event that take place in NGC 4656 (∼200–300 Myr, see Section 6.4). Therefore, the rotational motion in NGC 4656 has not be able to homogenize the metal content in this galaxy, regardless the mechanism that produce the azimuthal chemical inhomogeneities.

Our oxygen abundance values for NGC 4656 obtained with the N2 index (Marino et al. 2013) are very similar to those found by Zasov et al. (2017) doing the analysis with the same method, and are also similar to the values derived from Zasov et al. (2017) with theoretical IZI method. However, we found discrepancies with the abundances derived by previous authors when using the S method. In this paper, we do not find strong drops in the metallicities along NGC 4656 (variations of the order of 0.3 dex or greater) as previously found by Zasov et al. (2017), who suggests that these drops can be associated with a gas accretion event (Sánchez Almeida et al. 2014, 2015; Ceverino et al. 2016).

Considering the results mentioned above, the following questions arise: why do metals are distributed almost homogeneously in the north-east sector of NGC 4656, and what is the reason for the lower metallicity in the south-west sector of the galaxy? The metallicity distribution and the presence of large H II regions in the north-east region of the galaxy suggest the existence of gas flows which are induced by the gravitational interaction with its companions (NGC 4631 and mainly with NGC 4656UV). In this way, in agreement with simulations simulations (e.g. Rupke et al. 2010a) and the study of Pilyugin et al. (2015), the gas mixture would produce a flattening in the metal distribution of interacting systems. These gas flows would also explain the non-rotational motions evidenced in the radial velocity maps (presented in Fig. 15, Section 5.6.2). The south-west region of the galaxy, according to this scenario, would not be under the influence of strong gas flows as it happens in the north-east sector.

6.3 Star formation

The $\mathrm{SFRs}_{\mathrm{H}\alpha}$ obtained for NGC 4656 and NGC 4656UV, taking into account their uncertainties, locate both galaxies in the star-forming sequence of galaxies considering the relations published by Zahid et al. (2012) ($\log(M_*) \sim 8.5$–10.4) and McGaugh et al. (2017) ($\log(M_*) \sim 6.7$–9.8), respectively, confirming their late-type nature. We also found that the $\mathrm{SFR}_{\mathrm{H}\alpha}$ estimated for NGC 4656 is ∼3 times lower than the $\mathrm{SFR}_{\mathrm{FUV}}$ obtained by Schechtman-Rook & Hess (2012), and for NGC 4656UV the $\mathrm{SFR}_{\mathrm{H}\alpha}$ is ∼4 times lower than $\mathrm{SFR}_{\mathrm{FUV}}$. Among the possible reasons of this discrepancy, we can list (1) variations in the IMF that cause a deficiency of massive ionizing stars in low-mass galaxies, as suggested by Lee et al. (2009), who found that at low masses the luminosity in FUV is a better tracer of star formation compared to Hα, since the latter tends to underestimate the total SFR with respect to FUV, as lower-luminosity dwarf galaxies are examined, (2) the uncertainties caused by the indirect calibration of the FP cubes from the GMOS data (RMSE $= 1.32 \times 10^{-15}$ erg s^{-1} cm^{-2}, see Section 2.3.2).

On the other hand, we compared the $\mathrm{SFRs}_{\mathrm{H}\alpha}$ in the A, B, and C zones of NGC 4656, obtaining the highest $\mathrm{SFR}_{\mathrm{H}\alpha}$ in the A sector (∼2 times higher than in C) that indicates an enhancement in the star formation at the north region of this galaxy. It does not seem coincidence that this enhancement occurs closest to NGC 4656UV, where gas flows may be present. On the other hand, the south-west region has the lowest star formation activity, which could be produced by a low H I gas density, which is confirmed in the H I maps presented by Schechtman-Rook & Hess (2012, fig. 2). This suggests that NGC 4656UV would be primarily responsible for increasing the star formation in the north of NGC 4656 (rather than NGC 4631), where the reasons are explained in the next subsection.

6.4 Possible origin for NGC 4656UV

The origin of NGC 4656UV is unclear. Indeed, there are two studies that have proposed different scenarios regarding its nature. One of them is Schechtman-Rook & Hess (2012), who proposes that NGC 4656UV has been formed from a recent interaction between NGC 4656 and NGC 4631 (∼230 Myr ago), mainly based on the small difference between both radial velocities (40 km s^{-1}), in the filamentary structures of H I that arise from NGC 4631 to NGC 4656 (found by Weliachew et al. 1978; Rand 1994), and in the continuity of the the rotation gradient observed in the H I maps of NGC 4656. However, for that kind of interactions we would expect to find more tidal characteristics in the H I structure that surrounds NGC 4656 than those observed (Combes 1978; Martínez-Delgado et al. 2015). Also, there are no stellar tidal/bridges features connecting both galaxies or other optical evidence that indicate a previous baryonic interaction between NGC 4656 and NGC 4631 (Stayton et al. 1983). For example, Martínez-Delgado et al. (2015) discovered a giant stellar tidal stream in the halo of NGC 4631, which extends between NGC 4631 and NGC 4656; however, these authors rule out that the origin of this stellar stream was produced by an interaction between NGC 4631 and NGC 4656 due to the orientation of this structure with respect to the orientations of the two galaxies, indicating that the most likely origin is the interaction between NGC 4631 and its satellites. On the other hand, the continuity of the rotation between NGC 4656 and NGC 4656UV found by Schechtman-Rook & Hess (2012) does not necessarily indicate that NGC 4656UV is part of

the structure of NGC 4656. Similar is the case of the Magellanic Clouds, where both galaxies are inside a common H I envelope and are also connected in velocity (Brüns et al. 2005), which is an evidence the the ongoing interaction between both galaxies. By fitting the SED of NGC 4656UV, Schechtman-Rook & Hess (2012) find that its metallicity is approximately 10 times lower than the value reported for NGC 4656 ([Fe/H] ~ -1.12; Mapelli et al. 2010), thus relating the origin of NGC 4656UV with a possible star formation event associated with gas located in the outskirts of NGC 4656. However, in this work we do not find that difference. We have estimated an oxygen abundance for NGC 4656UV of $12 + \log(\mathrm{O/H}) \sim 8.2$ which is similar to that obtained for NGC 4656, considering the uncertainties ($12 + \log(\mathrm{O/H}) \sim 8.1$). We have also estimated an abundance gradient for NGC 4656. If we extrapolate this gradient at large radius, we find that the oxygen abundance is 10 times lower than the central region at a radius of 300 kpc, which is not realistic (under the assumption that the abundance gradient can be extrapolated to large radius).

Recently, Zasov et al. (2017) used long-slit spectroscopy to obtain the kinematical parameters and the metallicity of NGC 4656UV and NGC 4656. They estimated the total dynamical mass of NGC 4656UV, concluding that this is an LSB dwarf galaxy, dominated by dark matter. They propose that the recent star formation in NGC 4656UV, responsible for its blue colour, is probably the result of the accretion of low-metallicity gas from NGC 4631. The same gas accretion could be feeding the north-east part of NGC 4656. As mentioned previously, based on our results of chemical abundances, in this work we do not find clear signs that indicate an accretion of gas from an external source.

Among our results, we found that the oxygen abundance for NGC 4656UV ($12 + \log(\mathrm{O/H}) \sim 8.2$) is very similar to that of NGC 4656 ($12 + \log(\mathrm{O/H}) \sim 8.1$) considering the uncertainties ($\sim$0.2 dex), which could indicate that both galaxies are forming stars from already enriched material, giving evidence in favour of a tidal origin for NGC 4656UV. However, it is also necessary to note that NGC 4656UV follows the MZR for dwarf galaxies of Jimmy et al. (2015) (within the dispersion of the relation). In this sense, NGC 4656UV does not have a high metallicity for its mass, which characterizes the TDGs (Weilbacher, Duc & Fritze-v. Alvensleben 2003).

Another possibility for the tidal origin of NGC 4656UV is that it could have been formed through the interaction between NGC 4656 and NGC 4657. However, as explained above, we found that NGC 4656 consists of only one galaxy. Although in this work we cannot rule out any scenario, and given the extreme complexity of the system, we propose that NGC 4656 and NCG 4656UV are a pair of interacting galaxies belonging to the NGC 4631 group, being the TDG candidate (NGC 4656UV) an LSB galaxy (with central magnitude 24 mag arsec^{-1}; Zasov et al. 2017) companion of NGC 4656, not of tidal origin but rather primordial. An eventual interaction between NGC 4656 and NCG 4656UV could have triggered the star formation in NGC 4656UV around 200 Myr ago, which is indicated by its UV emission. The weak Hα emission in NGC 4656UV suggests that this object is not experiencing an intense star-formation episode.

7 SUMMARY AND CONCLUSIONS

In this paper, we performed a spectroscopic and kinematic study of the interacting system NGC 4656/4656UV, through Gemini/GMOS data in multislit mode and FP data cubes, respectively, in order to find the possible origin of NGC 4656UV, a TDG candidate located in the north-east side of NGC 4656. We obtained a low chemical abundance for NGC 4656UV ($12 + \log(\mathrm{O/H}) \sim 8.2$), which follows the MZR for normal dwarf galaxies of Jimmy et al. (2015). For NGC 4656 (12+log(O/H)$\sim$8.1), we estimated the oxygen abundance gradient of the north-east region, where most of the H II regions are located, obtaining a flat gradient ($\beta = -0.027 \pm 0.029$ dex kpc^{-1}). This is in agreement with the abundance gradients obtained in literature for other irregular dwarf galaxies (Hunter & Hoffman 1999; van Zee & Haynes 2006; Croxall et al. 2009). In this work, we suggest that there are gas flows induced by the gravitational interaction between NGC 4656 and NGC 4631 and mainly with NGC 4656UV, which causes a mixture of gases and consequently a flattening of the gradient, consistent with simulations (Montuori et al. 2010; Rupke et al. 2010a; Torrey et al. 2012) and the study of Pilyugin et al. (2015) for irregular dwarf galaxies.

The FP kinematic data showed us the complexity of the system. Thanks to the spatial/spectral resolution of these data, we were able to obtain new and detailed results about the behaviour of the ionized gas in NGC 4656. Through the analysis of the radial velocity profiles and by fitting a kinematic model of the observed FP velocity field, we conclude that NGC 4656 consists of only one entity, and not two as was proposed by other authors (de Vaucouleurs & de Vaucouleurs 1964; Nilson 1973). From the kinematic model, we estimated for NGC 4656 a dynamical mass of $6.8^{1.8}_{-0.6} \times 10^9\,\mathrm{M}_\odot$ at an $R = 12.1$ kpc. The velocity field in NGC 4656 suggests that this galaxy is dominated by rotation ($V_{\max}/\sigma \gtrsim 2.8$); however, at small scales we find non-rotational and counter-rotating motions, which agrees with the results of Schechtman-Rook & Hess (2012) for the H I gas.

Based on the results found in this work, supplemented with information from the literature, we suggest that NGC 4656 and NCG 4656UV are a pair of interacting galaxies belonging to the NGC 4631 group, with NGC 4656UV being an LSB galaxy (with central magnitude 24 mag arsec^{-1}; Zasov et al. 2017), companion of NGC 4656, not of tidal origin but rather primordial. Its interaction with NGC 4656 triggered the star formation in NGC 4656UV; however, the weak emission in Hα suggests that this object is not experiencing an episode of intense star formation. Future studies of stellar populations based on IFS data are necessary to confirm this scenario.

ACKNOWLEDGEMENTS

Based on observations taken at the OHP (France), operated by the French CNRS. Based on data collected at the Gemini Observatory, which is operated by the Association of Universities for Research in Astronomy, Inc., under a cooperative agreement with the NSF on behalf of the Gemini partnership: the National Science Foundation (United States), the National Research Council (Canada), CONICYT (Chile), Ministerio de Ciencia, Tecnología Innovación Productiva (Argentina), and Ministério da Ciência, Tecnologia e Inovaçõ (Brazil). NM-E acknowledges the financial support of the Dirección de Investigación of the Universidad de La Serena, through a 'Concurso de Apoyo a Tesis 2015', under contract PT1541. ST-F acknowledges the financial support of DIDULS project PR16143. NM-E and FU-V acknowledges the financial support of the project CONICYT PAI 82140065. JAHJ thanks to Brazilian institution CNPq for financial support through postdoctoral fellowship (project 150237/2017-0). The authors thank Benoît Epinat, Michel Marcelin, Jean-Luc Gach, and Olivier Boissin for having made possible the OHP observations using the GHASP team instrument. In particular, we thank Benoît Epinat for optimizing the observational strategy to minimize ghosts due to parasitic reflections.

REFERENCES

Amram P., Plana H., Mendes de Oliveira C., Balkowski C., Boulesteix J., 2003, A&A, 402, 865
Amram P., Mendes de Oliveira C., Plana H., Balkowski C., Hernandez O., 2007, A&A, 471, 753
Arribas S., Colina L., Bellocchi E., Maiolino R., Villar-Martín M., 2014, A&A, 568, A14
Baldwin J. A., Phillips M. M., Terlevich R., 1981, PASP, 93, 5
Bell E. F., McIntosh D. H., Katz N., Weinberg M. D., 2003, ApJS, 149, 289
Bertola F., Bettoni D., Danziger J., Sadler E., Sparke L., de Zeeuw T., 1991, ApJ, 373, 369
Bothun G. D., 1994, in Shlosman I., ed., Mass-Transfer Induced Activity in Galaxies, Cambridge Univ. Press, Cambridge. p. 218
Boulesteix J., 1993, ADHOC Reference Manual, Publications de l'Observatoire de Marseille, Marseille
Bournaud F., 2010, Adv. Astron., 2010
Bournaud F., Powell L. C., Chapon D., Teyssier R., 2011, in Brummell N. H., Brun A. S., Miesch M. S., Ponty Y., eds, Proc. IAU Symp. 271, Astrophysical Dynamics: From Stars to Galaxies, Cambridge Univ. Press, Cambridge, p. 160 (arXiv:1012.5227)
Bresolin F., Kennicutt R. C., 2015, MNRAS, 454, 3664
Bresolin F., Schaerer D., González Delgado R. M., Stasińska G., 2005, A&A, 441, 981
Bresolin F., Kennicutt R. C., Ryan-Weber E., 2012, ApJ, 750, 122
Brüns C. et al., 2005, A&A, 432, 45
Burbidge E. M., Burbidge G. R., Shelton J. W., 1967, ApJ, 150, 783
Calzetti D., Armus L., Bohlin R. C., Kinney A. L., Koornneef J., Storchi-Bergmann T., 2000, ApJ, 533, 682
Ceverino D., Sánchez Almeida J., Muñoz Tuñón C., Dekel A., Elmegreen B. G., Elmegreen D. M., Primack J., 2016, MNRAS, 457, 2605
Combes F., 1978, A&A, 65, 47
Croxall K. V., van Zee L., Lee H., Skillman E. D., Lee J. C., Côté S., Kennicutt R. C., Jr, Miller B. W., 2009, ApJ, 705, 723
Daigle O., Carignan C., Hernandez O., Chemin L., Amram P., 2006, MNRAS, 368, 1016
de Mello D. F., Urrutia-Viscarra F., Mendes de Oliveira C., Torres-Flores S., Carrasco E. R., Cypriano E., 2012, MNRAS, 426, 2441
De Robertis M. M., Dufour R. J., Hunt R. W., 1987, JRASC, 81, 195
de Vaucouleurs G., de Vaucouleurs A., 1964, ApJ, 140, 1622
Denicoló G., Terlevich R., Terlevich E., 2002, MNRAS, 330, 69
Domínguez A. et al., 2013, ApJ, 763, 145
Duc P.-A., 2012, Astrophys. Space Sci. Proc., 28, 305
Duc P.-A., Mirabel I. F., 1998, A&A, 333, 813
Duc P.-A., Mirabel I. F., 1999, in Barnes J. E., Sanders D. B., eds, Proc. IAU Symp. 186, Galaxy Interactions at Low and High Redshift, Kluwer, Dordrecht. p. 61
Duc P.-A., Ferrarese L., Cuillandre J.-C., Gwyn S., MacArthur L. A., Ferriere E., Côté P., Durrell P., 2011, in Koleva M., Prugniel P., Vauglin I., eds, EAS Publ. Ser. Vol. 48, Faint Dwarf Galaxies in the Next Generation Virgo Cluster Survey, EDP Sciences, France. p. 345 (arXiv:1010.3513)
Duc P.-A., Paudel S., McDermid R. M., Cuillandre J.-C., Serra P., Bournaud F., Cappellari M., Emsellem E., 2014, MNRAS, 440, 1458
Epinat B., Amram P., Marcelin M., 2008, MNRAS, 390, 466
Fitzpatrick E. L., 1999, PASP, 111, 63
Gach J.-L. et al., 2002, PASP, 114, 1043
Garrido O., Marcelin M., Amram P., Balkowski C., Gach J. L., Boulesteix J., 2005, MNRAS, 362, 127
Gooch R., 1996, in Jacoby G. H., Barnes J., eds, ASP Conf. Ser. Vol. 101, Astronomical Data Analysis Software and Systems V. Astron. Soc. Pac., San Francisco, p. 80
Hibbard J. E., van Gorkom J. H., 1996, AJ, 111, 655
Ho I. et al., 2018, preprint (arXiv:1807.02043)
Ho I.-T. et al., 2017, ApJ, 846, 39
Hook I. M., Jørgensen I., Allington-Smith J. R., Davies R. L., Metcalfe N., Murowinski R. G., Crampton D., 2004, PASP, 116, 425
Hunsberger S. D., Charlton J. C., Zaritsky D., 1996, ApJ, 462, 50
Hunter D. A., Hoffman L., 1999, AJ, 117, 2789
Jimmy Tran K.-V., Saintonge A., Accurso G., Brough S., Oliva-Altamirano P., 2015, ApJ, 812, 98
Kauffmann G., White S. D. M., 1993, MNRAS, 261
Kauffmann G. et al., 2003, MNRAS, 346, 1055
Kennicutt R. C., Jr, 1998, ARA&A, 36, 189
Kennicutt R. C., Jr, Keel W. C., Blaha C. A., 1989, AJ, 97, 1022
Kewley L. J., Ellison S. L., 2008, ApJ, 681, 1183
Kewley L. J., Dopita M. A., Sutherland R. S., Heisler C. A., Trevena J., 2001, ApJ, 556, 121
Kewley L. J., Rupke D., Zahid H. J., Geller M. J., Barton E. J., 2010, ApJ, 721, L48
Krabbe A. C., Rosa D. A., Dors O. L., Pastoriza M. G., Winge C., Hägele G. F., Cardaci M. V., Rodrigues I., 2014, MNRAS, 437, 1155
Kravtsov A. V., Klypin A. A., Bullock J. S., Primack J. R., 1998, ApJ, 502, 48
Kudritzki R. P., Castro N., Urbaneja M. A., Ho I.-T., Bresolin F., Gieren W., Pietrzyński G., Przybilla N., 2016, ApJ, 829, 70
Lee H., Skillman E. D., Cannon J. M., Jackson D. C., Gehrz R. D., Polomski E. F., Woodward C. E., 2006, ApJ, 647, 970
Lee J. C. et al., 2009, ApJ, 706, 599
López-Hernández J., Terlevich E., Terlevich R., Rosa-González D., Díaz Á., García-Benito R., Vílchez J., Hägele G., 2013, MNRAS, 430, 472
Magrini L., Gonçalves D. R., Vajgel B., 2017, MNRAS, 464, 739
Makarov D., Karachentsev I., 2011, MNRAS, 412, 2498
Mapelli M., Ripamonti E., Zampieri L., Colpi M., Bressan A., 2010, MNRAS, 408, 234
Marino R. A. et al., 2013, A&A, 559, A114
Martínez-Delgado D., D'Onghia E., Chonis T. S., Beaton R. L., Teuwen K., GaBany R. J., Grebel E. K., Morales G., 2015, AJ, 150, 116
Matteucci F., 2012, Astronomy and Astrophysics Library, Chemical Evolution of Galaxies. Springer, Berlin
McGaugh S. S., Schombert J. M., Lelli F., 2017, ApJ, 851, 22
Moiseev A. V., Tikhonov A. V., Klypin A., 2015, MNRAS, 449, 3568
Montuori M., Di Matteo P., Lehnert M. D., Combes F., Semelin B., 2010, A&A, 518, A56
Mould J. R. et al., 2000, ApJ, 529, 786
Moustakas J., Kennicutt R. C., Jr, 2006, ApJS, 164, 81
Moustakas J., Kennicutt R. C., Jr, Tremonti C. A., Dale D. A., Smith J.-D. T., Calzetti D., 2010, ApJS, 190, 233
Nilson P., 1973, Uppsala general catalogue of galaxies, Vol. 6, Astronomiska Observatorium, Uppsala
Nordsieck K. H., 1973, ApJ, 184, 719
Olave-Rojas D., Torres-Flores S., Carrasco E. R., Mendes de Oliveira C., de Mello D. F., Scarano S., 2015, MNRAS, 453, 2808
Osterbrock D., Ferland G., 2006, Astrophysics Of Gas Nebulae and Active Galactic Nuclei, 2nd edn. Univ. Sci. Books, Sausalito, CA
Pérez-Montero E., Díaz A. I., 2005, MNRAS, 361, 1063
Pilyugin L. S., Izotova I. Y., Sholudchenko Y. S., 2008, Kinematics Phys. Celest. Bodies, 24, 192
Pilyugin L. S., Grebel E. K., Mattsson L., 2012, MNRAS, 424, 2316
Pilyugin L. S., Grebel E. K., Kniazev A. Y., 2014, AJ, 147, 131
Pilyugin L. S., Grebel E. K., Zinchenko I. A., 2015, MNRAS, 450, 3254
Ploeckinger S., Recchi S., Hensler G., Kroupa P., 2015, MNRAS, 447, 2512
Rand R. J., 1994, A&A, 285, 833
Rich J. A., Torrey P., Kewley L. J., Dopita M. A., Rupke D. S. N., 2012, ApJ, 753, 5
Roberts M. S., 1968, ApJ, 151, 117
Rosa D. A., Dors O. L., Krabbe A. C., Hägele G. F., Cardaci M. V., Pastoriza M. G., Rodrigues I., Winge C., 2014, MNRAS, 444, 2005
Rosado M., Gabbasov R. F., Repetto P., Fuentes-Carrera I., Amram P., Martos M., Hernandez O., 2013, AJ, 145, 135
Roy J.-R., Kunth D., 1995, A&A, 294, 432
Rupke D. S. N., Kewley L. J., Barnes J. E., 2010a, ApJ, 710, L156
Rupke D. S. N., Kewley L. J., Chien L.-H., 2010b, ApJ, 723, 1255
Salim S., Lee J. C., Ly C., Brinchmann J., Davé R., Dickinson M., Salzer J. J., Charlot S., 2014, ApJ, 797, 126
Sánchez Almeida J., Morales-Luis A. B., Muñoz-Tuñón C., Elmegreen D. M., Elmegreen B. G., Méndez-Abreu J., 2014, ApJ, 783, 45

Sánchez Almeida J. et al., 2015, ApJ, 810, L15
Sánchez S. F. et al., 2014, A&A, 563, A49
Scarano S., Madsen F. R. H., Roy N., Lépine J. R. D., 2008, MNRAS, 386, 963
Schechtman-Rook A., Hess K. M., 2012, ApJ, 750, 171
Seth A. C., Dalcanton J. J., de Jong R. S., 2005, AJ, 129, 1331
Sorce J. G., Tully R. B., Courtois H. M., Jarrett T. H., Neill J. D., Shaya E. J., 2014, MNRAS, 444, 527
Stayton L. C., Angione R. J., Talbert F. D., 1983, AJ, 88, 602
Toomre A., Toomre J., 1972, ApJ, 178, 623
Torres-Flores S., Epinat B., Amram P., Plana H., Mendes de Oliveira C., 2011, MNRAS, 416, 1936
Torres-Flores S., Scarano S., Mendes de Oliveira C., de Mello D. F., Amram P., Plana H., 2014, MNRAS, 438, 1894
Torrey P., Cox T. J., Kewley L., Hernquist L., 2012, ApJ, 746, 108
Tremonti C. A. et al., 2004, ApJ, 613, 898
van der Kruit P. C., Allen R. J., 1978, ARA&A, 16, 103
van Dokkum P. G., 2001, PASP, 113, 1420
van Zee L., Haynes M. P., 2006, ApJ, 636, 214
van Zee L., Salzer J. J., Haynes M. P., O'Donoghue A. A., Balonek T. J., 1998, AJ, 116, 2805
Warner P. J., Wright M. C. H., Baldwin J. E., 1973, MNRAS, 163, 163
Weilbacher P. M., Duc P.-A., Fritze-v. Alvensleben U., 2003, A&A, 397, 545
Weliachew L., Sancisi R., Guelin M., 1978, A&A, 65, 37
Westmeier T., Koribalski B. S., Braun R., 2013, MNRAS, 434, 3511
Williams M. J., Bureau M., Cappellari M., 2010, MNRAS, 409, 1330
Zahid H. J., Dima G. I., Kewley L. J., Erb D. K., Davé R., 2012, ApJ, 757, 54
Zaritsky D., Kennicutt R. C. Jr. Huchra J. P., 1994, ApJ, 420, 87
Zasov A. V., Saburova A. S., Egorov O. V., Uklein R. I., 2017, MNRAS, 469, 4370
Zwicky F., 1956, Ergeb. der exakt. Naturw., 29, 344

This paper has been typeset from a TEX/LATEX file prepared by the author.